Chapter 5. Ocean Surface Waves and Spectra

Paris W. Vachon
Canada Centre for Remote Sensing, Natural Resources Canada, Ottawa, Ontario, Canada

Frank M. Monaldo
Johns Hopkins University Applied Physics Laboratory, Laurel, Maryland USA

Benjamin Holt
Jet Propulsion Laboratory, California Institute of Technology, Pasadena, California USA

Susanne Lehner
Deutsches Zentrum für Luft- und Raumfahrt, D-Wessling Germany

5.1 Introduction

Waves are the ocean's most obvious surface feature. Wavelengths can range from centimeters (for capillary waves or ripples) to hundreds of meters (for wind sea or swell) and wave heights can range from tiny perturbations of the ocean surface to tens of meters. Surface waves are generated by wind and turbulence in the atmosphere immediately above the ocean surface. Ocean surface waves interact with the atmosphere, ocean currents, the bottom topography, and with one another. Wave energy eventually dissipates through breaking in open water or upon shoaling.

There are many activities that require an understanding of the properties and characteristics of ocean surface waves in general, as well as their statistical properties for specific locations. Information on ocean surface waves has bearing on ocean engineering and structural design, ship design and navigation, prediction of and response to coastal processes, and the dissipation of marine pollution, to name just a few.

Measuring ocean surface waves from space may be one of the key contributions that satellites will make to further our understanding of the earth's oceans. If wave parameters such as wave height, wave length, and propagation direction can be obtained globally, fundamental knowledge of the generation and propagation of waves would become available and would provide a synoptic view of waves that is unattainable by buoys or ships. This knowledge would improve our understanding of the atmospheric forcing on the ocean surface, of the distribution of this energy across the ocean basins and downward into the water column through upper ocean mixing, and help to mitigate hazards to shipping and coastal regions .

Wave modeling is an important approach to generating and predicting ocean surface wave statistics. Operational wave models are driven by forecast wind fields and can include an update of the wave's initial conditions based upon both in-situ and remote sensing wave measurements. Remote sensing data can be used to improve the model's initial conditions, to verify forecast skill, and to provide insight into the physics that are implemented in the model.

Ocean surface waves are traditionally measured in-situ at a point on the ocean surface by averaging wave properties such as vertical and horizontal displacement over time as the waves propagate past a fixed location, such as a moored buoy. This approach can provide the directional distribution (i.e., in the direction of wave propagation) of wave energy at each wave frequency that is present, which constitutes the directional wave spectrum. Most wave buoys are near the coast and only a limited number measure wave propagation direction. Remote sensing, however, offers some alternate approaches. For sensors that provide an image of the waves, a spatial average is acquired at a fixed instant in time, rather than a temporal average at a fixed point in space. This approach can also provide the directional distribution of wave energy, but at each wavelength present rather than each frequency. In principle, the two approaches are related through the wave dispersion relation.

Synthetic aperture radar (SAR) is a unique sensor for ocean surface wave measurement since SAR is the only sensor that can provide images from space with high enough resolution, independent of cloud cover and light conditions, to detect ocean surface wave scales of interest. As first demonstrated from aircraft flights during the early to mid-1970s, the two-dimensional surface wave field can be imaged by SAR. A RADARSAT-1 SAR image of ocean surface waves refracting along a beach and around a headland is shown in Figure 5.1. The SEASAT mission in 1978 provided the first realization of extensive global ocean wave measurements from space, with the SAR providing directional wave information and the altimeter providing significant wave height.

Since the microwave backscatter is from the short scale ripples, the apparent modulation of the ripples by the longer waves renders the longer waves visible in the SAR image. If the waves are long and are not too high, the SAR imaging mechanisms may be linear and it is possible to directly estimate a directional wave spectrum from a SAR image spectrum. As this chapter will highlight, the motion of the waves during SAR data acquisition causes the imaging process to become non-linear as the waves become steeper (that is, for higher or shorter waves). In this case, the wave image and the derived wave spectrum could become distorted, with an important impact being a reduction in the ability of SAR to accurately sense the wave component in the along-track direction. A good understanding of the SAR wave imaging process was reached rather recently. The derivation of ocean surface wave properties from SAR images often benefits from non-linear inversion schemes that are constrained by wave data, usually taken from a wave forecast model. When SAR-derived ocean surface wave properties were combined with the extensive spaceborne SAR image data that became available in the early 1990s, a wide variety of SAR wave studies and applications ensued.

In this chapter, we first present an historical perspective on ocean surface wave measurement by SAR. We then present elementary ocean surface wave properties and discuss how SAR responds to them. Next we present examples of SAR image spectra and applications derived from several different SAR systems. Finally, we discuss the future prospects for ocean surface wave measurement from spaceborne SAR.

5.1.1 Historical Perspective

The most ambitious and uncertain instrument carried aboard the SEASAT satellite in 1978 was its SAR. In comparison to the other payload instruments, the SAR consumed large amounts of power and download bandwidth. There were additional technical challenges in processing the raw data into imagery, especially given the modest, at least by contemporary standards, computing power that was available. Up to that time, SAR images had largely been processed on optical benches. Even more fundamentally, there were real concerns and apprehensions as to what might be visible from a spacecraft SAR.

When SEASAT SAR imagery became available, it was clear that many phenomena, including internal waves, wind signatures, oil slicks, and ocean surface waves were visible [see *Beal et al.,* 1981; *Fu and Holt*, 1982; *Vesecky and Stewart*, 1982]. It was also clear that it would

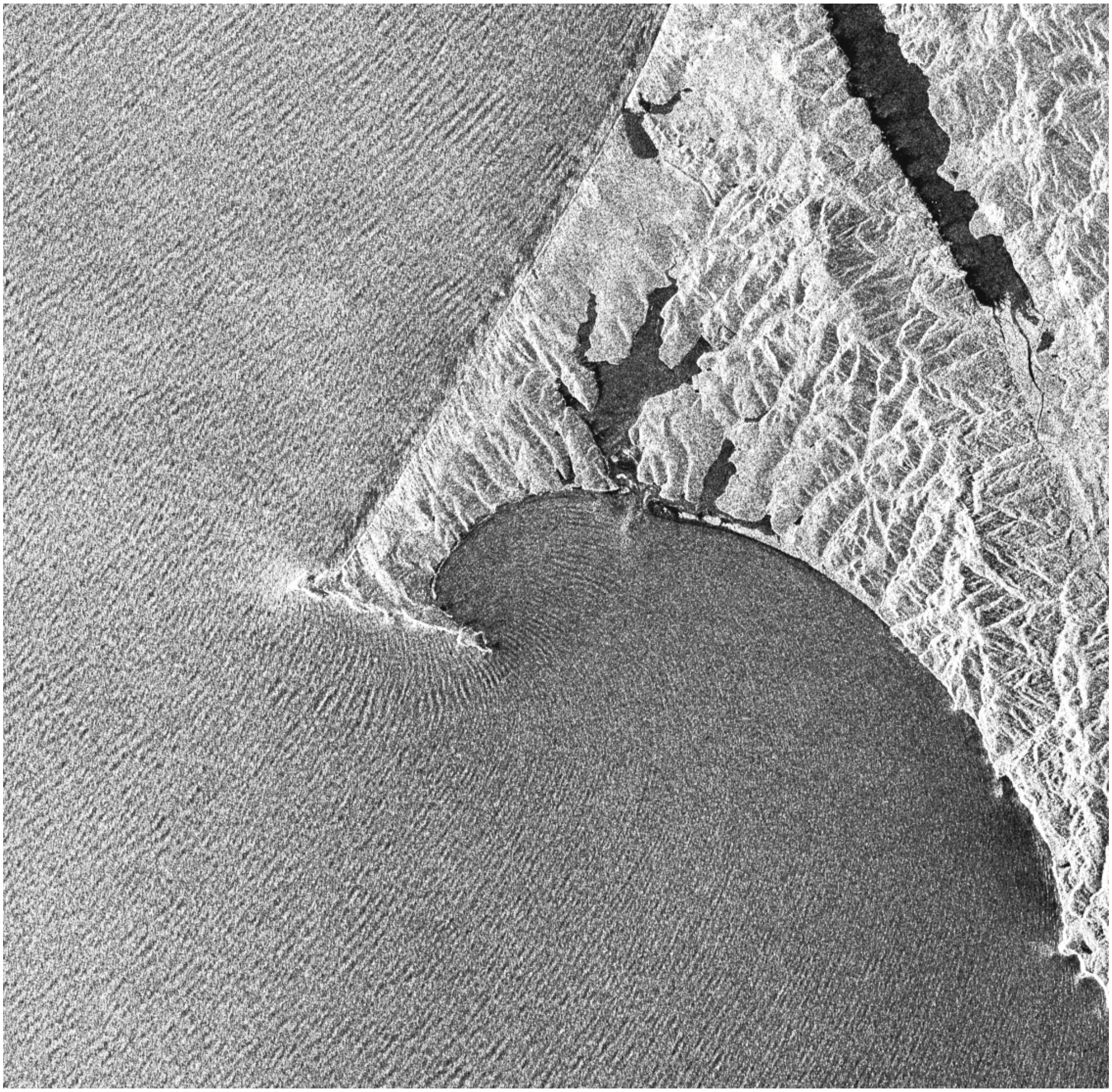

Figure 5.1. RADARSAT-1 (C-band, HH) S1 image from 22 November 2001 showing ocean surface waves refracting along Point Reyes Beach and around Point Reyes (the leftmost point), Point Reyes National Seashore, CA, USA. The imaged area is 31.5 km x 31.5 km. ©CSA 2001

take some time to acquire the skill and knowledge necessary to make quantitative ocean measurements from SAR imagery. Though the SEASAT satellite mission ended prematurely after only three months, it provided a wealth of data that would occupy researchers for years; SAR images of ocean surface waves continue to be an application of interest.

Gonzalez et al. [1980] and *Beal* [1980] looked in detail at the ocean surface wave detection capabilities of SEASAT. In particular, *Beal et al.* [1983] devoted considerable effort to measuring the spatial evolution of SEASAT SAR-measured wave spectra from a pass taken off the U.S. East Coast. The wavenumber of the dominant wave spectra was shown to have changed

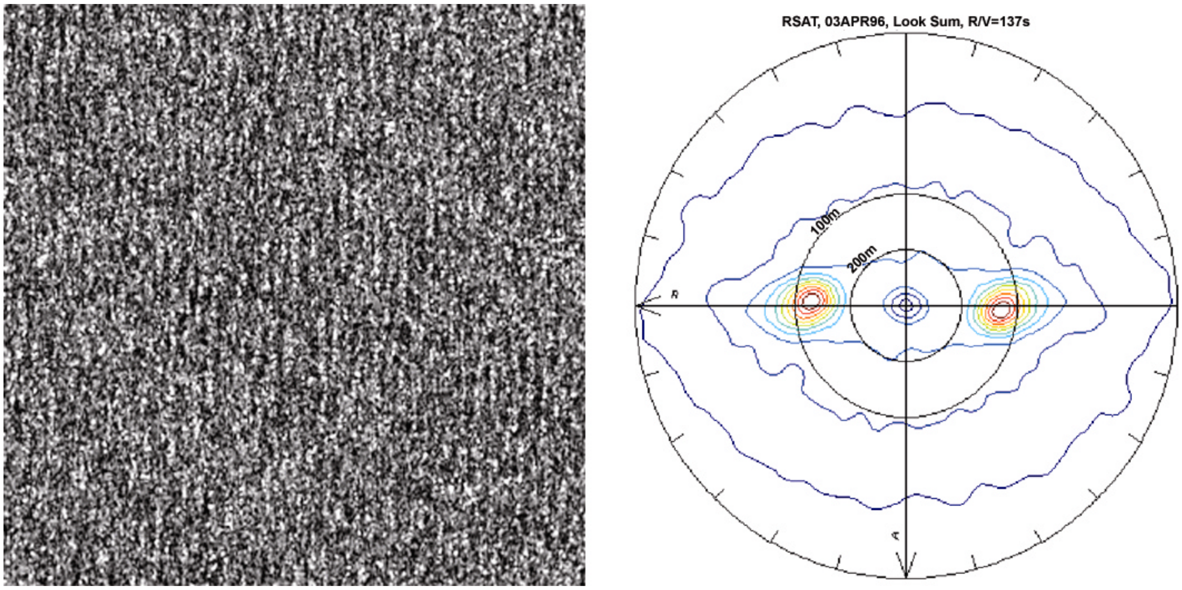

Figure 5.2. RADARSAT-1 (C-band, HH) SAR image (©CSA 1996) showing ocean waves (left) and the corresponding SAR image spectrum (right). The image covers 6.4 km by 6.4 km.

in a way that was consistent with deep-water wave dispersion as the waves propagated away from a storm and interacted with the Gulf Stream current.

Since SEASAT was short-lived, subsequent efforts to study SAR ocean surface wave measurement often focussed on airborne SARs [*e.g., Vachon et al.*, 1988] and remained largely anecdotal. In 1981 and 1984, SIR-A and SIR-B (Shuttle Imaging Radar) carried out one-week missions on the space shuttle *Challenger*. Perhaps the most capable SAR, with multiple frequencies (L-, C-, and X-bands) and polarizations, was launched for two, one-week missions in 1994 on the space shuttle *Endeavour* as part of the SIR-C/X-SAR mission. These missions were of interest since they provided very favorable acquisition geometry for ocean surface wave imaging. The SIR-C/X-SAR missions included a real time processor and downlink system for ocean surface wave measurement of the southern ocean (see Section 5.4.5).

In part due to the intriguing SEASAT results, SARs eventually found their way onto ERS-1 (1991), ERS-2 (1995), JERS-1 (1992), and RADARSAT-1 (1995). All of these but JERS-1 carry (or carried) C-band SARs and all have provided useful ocean surface wave information (*e.g.,* Figures 5.1 and 5.2). JERS-1 carried an L-band SAR, but an antenna problem forced a reduction in the transmitted power, which resulted in a poor signal-to-noise ratio for ocean images and rather limited ocean applications. The Soviet satellite ALMAZ carried an S-band SAR that also provided some ocean surface wave observations [*e.g., Tilley and Beal*, 1994].

The launch of ERS-1 by ESA in 1991 marked the advent of routine ocean surface wave spectra measurement from space via SAR images, or more specifically, via imagettes from the ERS wave mode of operation. For this mode, a full resolution imagette covering 5 km by 10 km is acquired every 200 km along track. This mode offers global coverage through available onboard data storage. Image spectra are then calculated from the imagettes and are distributed to weather forecasting centers on a quasi-operational schedule. These wave mode products have received considerable attention for the development of SAR inversion and assimilation algorithms [*e.g., Breivik et al.*, 1998; *Dunlap et al.*, 1998], as well as for wave applications on a basin scale [*e.g., Heimbach and Hasselmann*, 2000].

ERS-2 was launched in 1995 and provided continuity of coverage and modes with ERS-1. Canada's RADARSAT-1 was launched in 1995 and provided SAR ocean images with a more flexible geometry and on a commercial basis. The derivation of ocean surface wave parameters from RADARSAT-1 SAR images has also been considered [*e.g.*, *Dowd et al.*, 2001].

5.2 Elementary Ocean Surface Wave Properties

There are many elementary treatments of ocean surface wave properties available in the literature [*e.g., Pond and Pickard*, 1983]. In this chapter, we are interested in waves on the ocean surface that are generated by wind forcing. These wind waves propagate away from their source location as swell and eventually dissipate their energy through wave breaking in the open ocean (as white caps) or near the coast (as surf).

The irregular undulations of the ocean surface can be described mathematically as a sum of simple cosine-shaped waves with different amplitudes, relative phases, and frequencies. The wave spectrum is a decomposition of the surface wave component energy (proportional to the amplitude-squared) that is plotted as a function of wave frequency or wavenumber.

For waves that are not too steep (*i.e.,* the wave height is just a few percent of the wavelength), linear wave theory applies. A particular ocean surface wave component may be written as:

$$h = A\cos(kx - wt) \tag{1}$$

where A is the wave amplitude $k = 2p / \Lambda$ is the wavenumber, Λ is the wavelength, $w = 2p / T$ is the wave frequency, and T is the wave period. The argument $(kx - wt)$ is the wave phase, which varies from 0 to $2p$ in moving from one crest to the next at a fixed instant in time, or in waiting through one cycle of the wave at a fixed point in space. The phase speed is the speed of propagation of a wave crest and is given by $C = w / k$.

For freely propagating ocean surface waves, the wavenumber and wave frequency are not independent, but are linked through the wave dispersion relation:

$$w^2 = gk\tanh(kh) \tag{2}$$

where h is the water depth. For deep water (h >> Λ), $w = \sqrt{gk}$, $C = \sqrt{g/k}$, and we see that the waves are dispersive with longer waves travelling faster. This leads to wave groups that travel with group speed $C_g = dw/dk = C/2$.

The phase speed is a measure of the speed of travel of a point of constant phase (*e.g.,* the crest or trough) along a wave cycle. A particle of water on the ocean's surface, on the other hand, is subject to an orbital motion as the wave propagates past it. For deep water, the horizontal and vertical orbital motion components are given by:

$$\begin{aligned} u &= wA\cos(kx - wt) \\ v &= wA\sin(kx - wt) \end{aligned} \tag{3}$$

The top panel of Figure 5.3 shows a plot of the orbital velocity of a sinusoidal wave. A radar scatterer on the ocean surface follows a circular motion with orbital velocity given by (3).

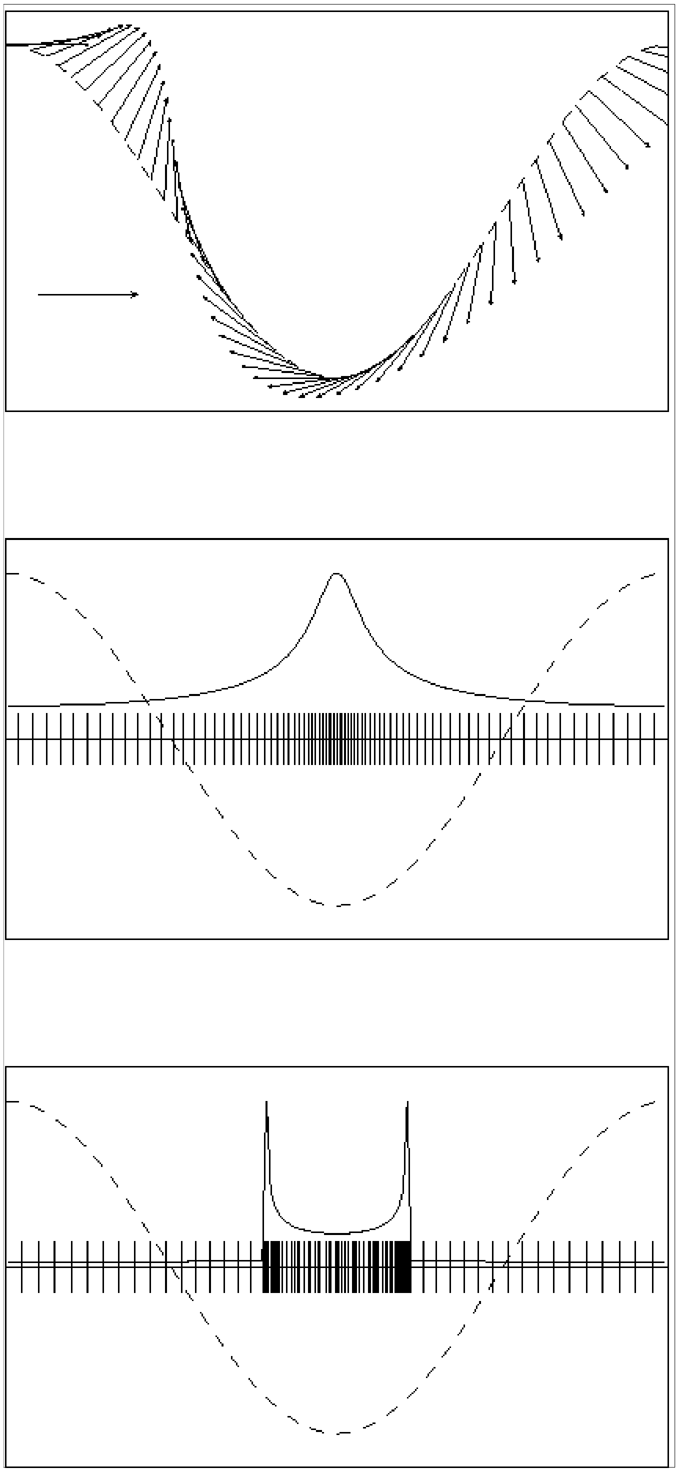

Figure 5.3. Conceptual diagram showing SAR velocity bunching image mapping. A single azimuth traveling wave cycle, moving left-to-right, is considered. The upper panel shows the orbital velocity that controls the velocity bunching. The middle panel shows a case of small nonlinearity. The scatterers are bunched in azimuth, with density, hence image contrast, shown by the solid curve. The lower panel shows a case of larger nonlinearity. In this case multiple peaks are produced in the image for each actual wave cycle

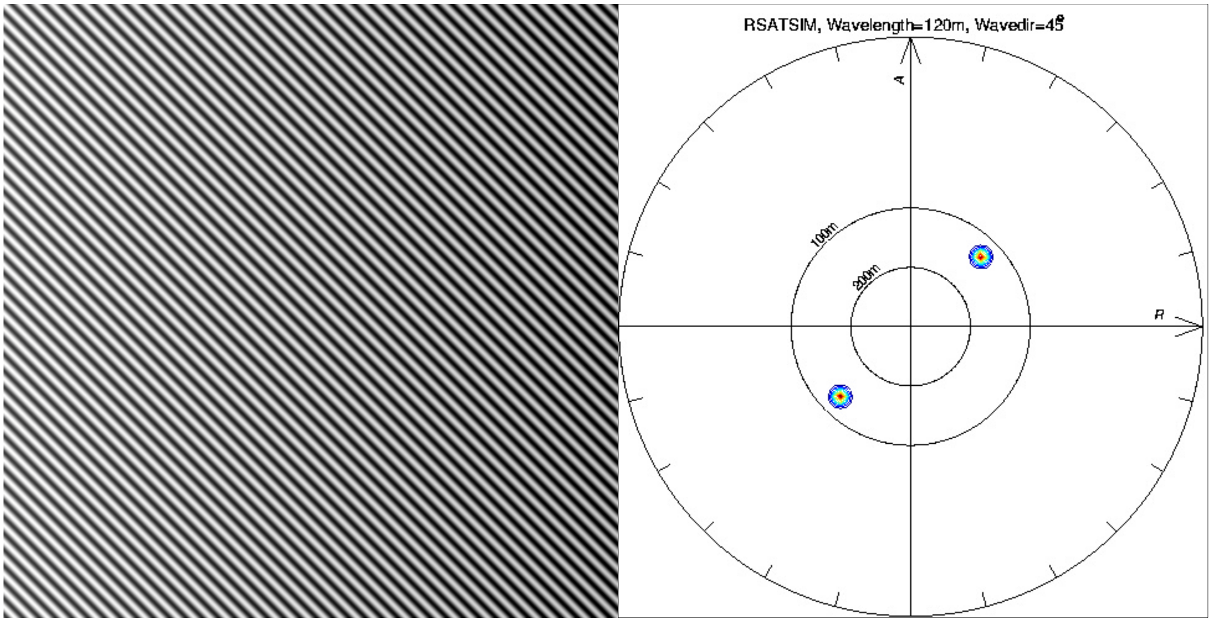

Figure 5.4. A simulated image of a sinusoidal wave (left) of 120 m wavelength traveling 45° off azimuth, and the corresponding image spectrum (right). The simulated image covers an area of 6.4 km by 6.4 km

An important wave field property is the significant wave height H_s, sometimes referred to as the sea state. Historically, H_s is defined as the average of the highest one-third of the observed waves. *Borgman* [1982] shows that, for a Gaussian wave height distribution, $H_s = 4\sqrt{\langle h^2 \rangle}$, or four times the standard deviation of the ocean surface displacement.

Ocean surface waves are usually measured as a time series of height displacements at a particular point, as with a moored wave buoy. The measurements may be gathered over a certain period of time and then a wave spectrum may be estimated as a function of wave frequency. On the other hand, a SAR provides an image of the waves at essentially a fixed instant of time. This spatial view allows the wave spectrum to be estimated as a function of wavenumber. These two approaches are related through the wave dispersion relation of (2).

5.2.1 Image Spectral Analysis

The use of SAR imagery for ocean surface wave measurement would be straightforward if the surface radar cross section were proportional to the ocean surface wave slope or wave height. In such an ideal case, simply computing the Fourier transform of a SAR image and computing the magnitude-squared of the result would produce an estimate of the two-dimensional ocean surface wave spectrum.

In Figure 5.4 we show an example of an ideal sinusoidal ocean surface wave image and its corresponding image spectrum. This example corresponds to a sinusoidal wind-wave with a wavelength of 120 m travelling 45º off the SAR's azimuth direction. The corresponding image spectrum contains the mapping of wavelength and direction that are present in the image. The circles of constant wavenumber (or alternately, circles of constant wave length) that are included on the spectrum allow a quick visual assessment of the wavelengths that are present. Note that the spectral peaks are located perpendicular to the crest orientation. Two peaks appear in the image spectrum since it is impossible to resolve the wave propagation direction by inspection of the image alone. As such, the energy in the image is split equally between the two possible propagation directions. Measurement of the peak location (k_x, k_y) allows estimation of the wave propagation direction as $\phi = \tan^{-1}(k_y, k_x)$ as well as estimation of the peak wavelength as $\Lambda = 2\pi / \sqrt{k_x^2 + k_y^2}$.

Under more generalized circumstances, there could be a distribution of wavelength components present, and indeed, several wave systems (*e.g.,* wind-waves and/or one or more swell components). As such, the resulting image spectrum would be distributed over the set of wavenumbers that are actually present.

For the spectral analysis of an actual SAR image, we first produce an image of relative image contrast. This is accomplished by dividing the image intensity by its mean value. It is worth noting that, as long as image intensity is proportional to radar cross section, radiometrically-calibrated imagery is not required for quantitative ocean surface wave analysis. Following spectral analysis, the starting point for estimation of ocean surface wave properties is the SAR image intensity-variance spectrum, $S_I\left(\vec{k}\right)$. An example of an ocean surface wave image and its corresponding SAR image spectrum was shown in Figure 5.2.

5.3 Wave Spectrum from SAR

5.3.1 Linear Transform

The first efforts to extract quantitative ocean surface wave spectral information from SAR imagery used a linear system approach in which the non-linear aspects of SAR imaging in the relationships between the surface waves and the radar cross section were simply ignored. Nonetheless, under certain circumstances such an approach can be used. The geometry of the SAR imaging process (for a flat earth and rectilinear platform motion) is shown in Figure 5.5. The local radar incident angle is θ and the propagation direction of the waves with respect to the SAR azimuth (*i.e.,* along track) direction is ϕ .

Elachi and Brown [1977] described some of the mechanisms that permit SARs to image ocean surface waves. In preparation for the launch of SEASAT, they explained that radar cross section variations were essentially proportional to wave slope variations. For side-looking radars, the radar cross section is proportional to the roughness on the surface at the scale of the radar wave length, typically on the order of a few centimeters or decimeters. In the "Bragg" scattering model, *Wright* [1960] showed that for a perfectly conducting rough surface, the radar cross section is given by:

$$\sigma^o = 16\pi k_0 (1 \pm \sin^2\theta)^2 \Psi(2k_0 \sin\theta) \tag{4}$$

where k_0 is the radar wavenumber and $\Psi(k)$ is the wave height-variance spectrum. The "plus" sign applies for vertical transmit and receive polarization while the "minus" sign applies for horizontal transmit and receive polarization. The short wave spectrum in this expression is evaluated at the Bragg wavelength, $2k_0 \sin\theta$, which is the projection of the radar wavenumber onto the local surface.

There are two ways that long ocean surface waves (longer than 50 m, for instance) can modify the radar cross section. The first is that the long waves modify the local surface angle

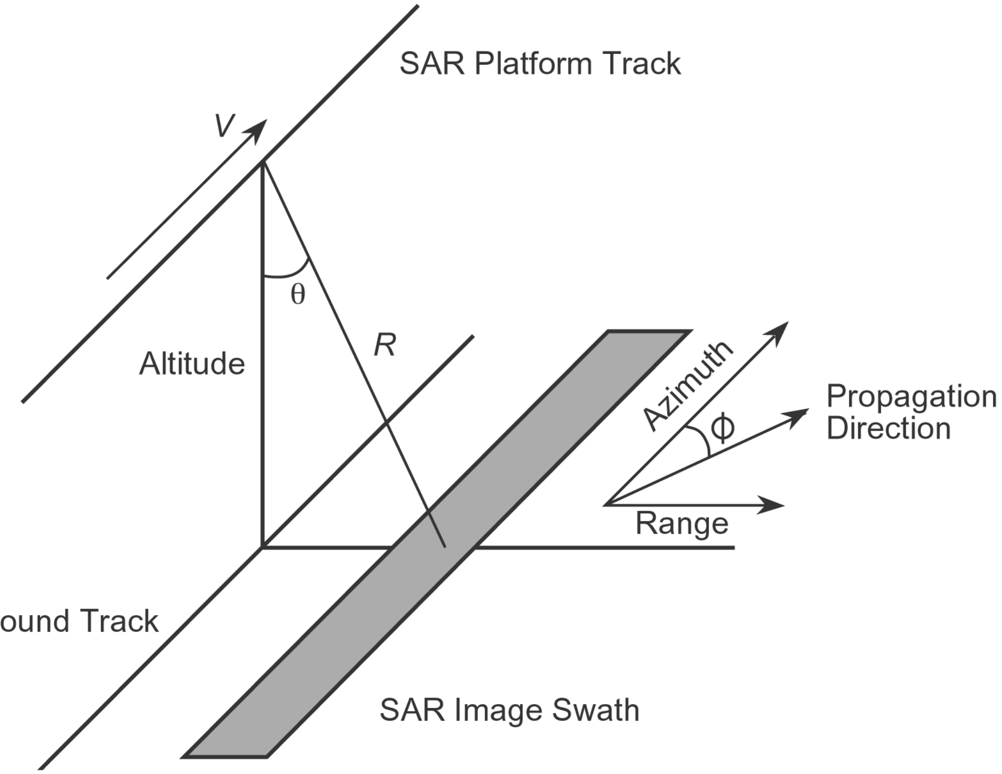

Figure 5.5. SAR ocean wave imaging geometry.

with respect to the angle of incidence. The second is for the long waves to hydrodynamically interact with the short Bragg-scale waves in such a way as to alter the roughness of the surface at the Bragg wavelength. This effect is called hydrodynamic modulation and it is still not particularly well modelled [*Alpers et al.,* 1981; *Hasselmann et al.,* 1985; *Engen et al.*, 2000].

These two mechanisms are most sensitive to wave components in the range direction, that is, those moving towards or away from the radar. *Alpers et al.* [1981] referred to these mechanisms as “real aperture radar” (RAR) modulation mechanisms because they apply equally well to real aperture and synthetic aperture radar images of the ocean surface.

There is a third modulation mechanism that is specific to SAR, allowing this class of radar to image ocean surface waves with an azimuth-traveling component. This mechanism is inherently linked to how a SAR creates a radar image. A SAR achieves its high resolution in the along track direction (azimuth) from the Doppler signal from the surface. As a SAR passes by a particular scatterer, the relative velocity, or Doppler shift, is measured. When the Doppler shift is zero, the azimuth position of the scatterer is assigned to the azimuth position of the SAR platform. However, if a scattering element has a velocity component u that is radial (*i.e.,* towards or away from the radar platform), this velocity component adds to the Doppler shift caused by the relative motion of the SAR platform. The consequence is that a scattering element moving towards the radar with velocity u has its apparent position in the SAR image shifted in the azimuth direction by $d = (R/V)u$. *Swift and Wilson* [1979] and *Alpers and Rufenach* [1979] explained how the periodic orbital motion of the ocean surface induces surface velocities that can shift the surface elements differentially in the azimuth direction in such a way as to increase and decrease the density of scattering elements in the SAR image. This variation in scatterer density, as illustrated in Figure 5.3, occurs at the spatial frequency of the long ocean surface waves, thus rendering them visible in the SAR image. This third mechanism for the SAR imaging of ocean surface waves is commonly known as velocity bunching modulation.

In principle, the relationship between the observed SAR image intensity-variance spectrum, $S_I\left(\vec{k}\right)$, and the ocean surface wave height-variance spectrum is given by

$$S_I\left(\vec{k}\right) = T\left(\vec{k}\right)\Psi\left(\vec{k}\right) \tag{5}$$

where $\Psi\left(\vec{k}\right)$ is the wave height-variance spectrum, $\vec{k}$ is the ocean surface wavenumber vector, and $T\left(\vec{k}\right)$ represents all of the modulation mechanisms that describe the mapping of an ocean surface wave spectrum into a SAR image spectrum. Equation (5) is a straightforward point-by-point matrix multiplication of the ocean surface wave spectrum and the modulation transfer function $T\left(\vec{k}\right)$. If $T\left(\vec{k}\right)$ can be completely specified, then it is possible to invert (5) in a straightforward way, and to estimate the wave height spectrum directly from the SAR image spectrum. The linear approximation here consists of assuming that we can estimate $T\left(\vec{k}\right)$ with no foreknowledge of the actual wave height spectrum. In practice, the derived $\Psi\left(\vec{k}\right)$ would contain the 180° propagation direction ambiguity.

5.3.2 Azimuth Cut-Off

SEASAT demonstrated that SAR could measure ocean surface waves from space, at least under certain circumstances. However, images from that sensor also revealed important limitations to SAR ocean surface wave imaging. While the orbital motion of longer ocean surface waves with an azimuth component allows the waves to be imaged through the velocity bunching mechanism, the random motions of the ocean surface caused by the shorter scale waves introduce random position shifts in azimuth that in turn degrade the azimuth resolution [*Harger*, 1970; *Raney*, 1971; *Raney*, 1980; *Raney and Vachon*, 1988]. This degraded azimuth resolution effectively introduces an azimuthal cut-off in the SAR-observed ocean surface wave spectrum. That is, the SAR cannot sense ocean surface wave components that are shorter than the cut-off wavelength.

This azimuthal cut-off effect grows monotonically with (R/V), the range-to-velocity ratio of the SAR platform, and with the sea state. The higher the satellite orbit, the higher the value of (R/V). For polar orbiting SARs that orbit the Earth at an altitude of about 800 km and for small incident angles, this parameter has a value of around 115 s. For the space shuttle, which orbits the Earth at an altitude of about 200 km, this parameter can be reduced by a factor of four. For airborne SARs, it is also possible to acquire ocean wave images with smaller values of (R/V).

The larger the value of (R/V) and the higher the wave height, the less able a SAR is to image ocean surface waves with an azimuth-traveling component. At typical ocean surface wave heights and for polar orbiting SARs, wave systems with wave lengths as long as 300 m traveling in the azimuth direction may not be visible [*Alpers et al.,* 1981; 1986; *Beal et al.*, 1983; *Monaldo and Beal*, 1986; *Tucker*, 1985]. *Beal et al.* [1983] proposed a semi-empirical relationship for the minimum detectable azimuth wavelength:

$$\Lambda_{\min} = \frac{R}{V}\sqrt{H_s} \tag{6}$$

where (R/V) is expressed in seconds and H_s is expressed in meters (there is an implied factor of unity with units m$^{1/2}$ s^{-1}). The azimuth cut-off is often modelled as an azimuth-oriented low-pass filter function (*e.g.,* Gaussian-shaped) of width Λ_{min}.

A number of approaches have been proposed to alleviate the azimuth cut-off problem. Since the ERS SARs have been making routine image spectra measurements through their wave mode, there has been considerable effort invested into using SAR measured image spectra in conjunction with wave models to improve ocean surface wave forecasts. Despite severely reduced response to the azimuth-traveling component of ocean surface waves, SAR image spectra were blended with wave spectra from wave models in a way that recognized that some of the wave systems might not be imaged. Indeed, much of the time, ocean surface waves have a component in the range direction (perpendicular to the satellite track) and useful information can be extracted [*Alpers*, 1983; *Alpers et al.,* 1986; *Hasselmann et al.,* 1991; *Vachon et al.*, 1994; *Heimbach et al.,* 1998; *Holt et al.*, 1998]. Such efforts require a more complete description of the non-linear aspects of SAR wave imaging to extend the wave retrieval fidelity.

5.3.3 Quasi-Linear Transform

We can write (5) more completely as:

$$S_I\left(\vec{k}\right) = \left[H_D\left(\vec{k}\right)T\left(\vec{k}\right)\Psi\left(\vec{k}\right) + S_N\left(\vec{k}\right)\right]. \tag{7}$$

The azimuth cut-off that is caused by random surface motion is represented by the dynamic response function, $H_D\left(\vec{k}\right)$, which is normally a function of Λ_{min}, which is in turn a function of the properties of the ocean surface wave spectrum itself. The $T\left(\vec{k}\right)$ term is called the SAR modulation transfer function and includes the effects of the tilt, hydrodynamic, and velocity modulation mechanisms. $S_N\left(\vec{k}\right)$ is added to the image spectrum to model the effect of speckle noise on the image spectrum. $S_N\left(\vec{k}\right)$ may be estimated from low contrast images produced by the same SAR and processor combination and is discussed further in the Section 5.3.4. Since the mapping between the ocean surface wave spectrum and the SAR image spectrum involves the properties of the ocean surface wave spectrum through $H_D\left(\vec{k}\right)$, the relation of (7) is often referred to as a quasi-linear transform [*e.g., Hasselmann and Hasselmann*, 1991; *Plant and Zurk*, 1997]. This transformation is more complete than (5) and is often adequate to describe the SAR imaging physics and can also be used in a straightforward way to estimate $\Psi\left(\vec{k}\right)$, provided that

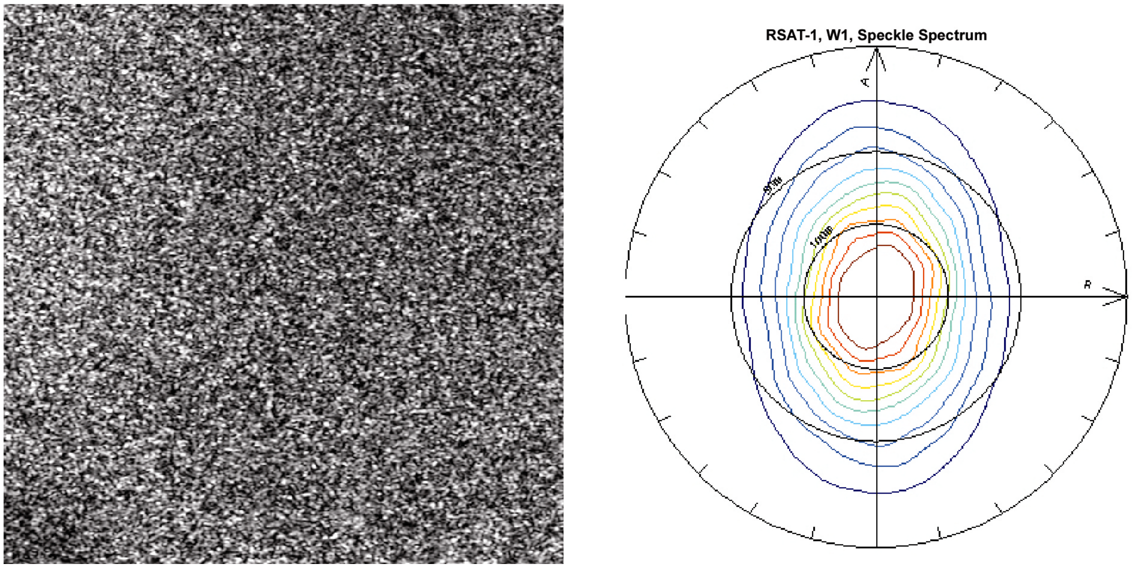

Figure 5.6. RADARSAT-1 (C-Band, HH) SAR image (©CSA 1996) showing image speckle (left) and the corresponding SAR image spectrum (right). The image covers an area of 6.4 km by 6.4 km.

all of the required matrices are available or can be modelled or estimated. In some cases, $H_D\left(\vec{k}\right)$ may be estimated from analysis of the azimuth structure of the observed SAR image spectrum, or can be based upon an external estimate of the wave conditions, from a wave forecast model, for example.

5.3.4 Speckle Noise

A SAR is a coherent imaging system, so speckle noise is an inherent property of the image. The speckle noise is correlated structure at the scale of the radar resolution. Multi-looking and image smoothing may be used to reduce this noise source at the expense of spatial resolution. In the spectral domain, speckle expresses itself as a broadband noise component. In the linear system model, a noise term, $S_N\left(\vec{k}\right)$, is added to the image spectrum to model the effect of speckle noise on the image spectrum [*Goldfinger*, 1982]. Spaceborne SARs often maintain high resolution at the expense of speckle noise; $S_N\left(\vec{k}\right)$ represent a significant and sometimes dominant contribution to the SAR image intensity-variance spectrum.

In Figure 5.6, we show a RADARSAT-1 SAR image of speckle noise, along with the corresponding image spectrum. In this case, the image is from a wind-roughened, enclosed body of water, which contains virtually no contrast. It is possible to further reduce the speckle contribution to the SAR image spectrum, but only at the expense of spatial resolution, which could compromise the ability to detect the wave scales of interest. Image spectra such as these have previously been used to examine the stationary response (*i.e.,* resolution) of various SARs and SAR processors [*Tilley*, 1986]. In practice, $S_N\left(\vec{k}\right)$ may be estimated from the image spectrum in spectral regions that don't contain any wave energy (*e.g.,* outside of the azimuth pass band). The inter-look cross spectrum technique, which will be discussed in a Section 5.3.7, allows calculation of an image contrast spectrum with a significantly reduced speckle noise component.

5.3.5 Limitation of Polar Orbiting SAR

In principle, by using the linear approximation of (7) and a measured SAR image spectrum, we can solve for the corresponding ocean surface wave slope spectrum. Another use for (7) is to study SAR geometries that allow the imaging of ocean surface waves with the best possible fidelity. Figure 5.7 contains plots of the total SAR transfer function as a function of range and azimuth wavenumbers, composed of $H_D\left(\vec{k}\right)T\left(\vec{k}\right)$, which relate a wave slope spectrum to a SAR image spectrum. Figure 5.7a represents the SIR (*i.e.,* space shuttle) geometries for low sea states. Note that, for wavelengths less than about 100 m, the transfer function is essentially constant. Hence, for this geometry, the SAR image spectrum is roughly proportional to the ocean surface wave slope spectrum. In this case, it is rather straightforward to interpret SAR image spectra as ocean surface wave spectra. Similar improvements in ocean surface wave imaging fidelity have been demonstrated for airborne SARs operated with a small $\left(R/V\right)$ [*e.g., Vachon et al.*, 1994].

On the other hand, when we increase the spacecraft altitude to 800 km, similar to the altitudes of SEASAT, ERS-1/2, JERS-1, RADARSAT-1, and ENVISAT in their polar orbits, we find that $\left(R/V\right) > 115$ s (becoming as large as 155 s for the outer beams of RADARSAT-1) and the transfer function is not nearly as benign as for smaller R/V (see Figure 5.7b). The response for the azimuth wavenumber component is severely degraded. This lack of azimuth response arises for all polar orbiting SARs since they orbit the earth at an altitude of roughly 800 km; a linear transform is certainly not suitable, and the suitability of a quasi-linear transform is limited to rather low sea states. This has motivated interest in non-linear techniques for retrieval of wave spectra from SAR imagery.

5.3.6 Non-Linear Transform

By the mid 1980s, a general consensus had emerged on the nature of SAR ocean surface wave imaging [*Hasselmann et al.,* 1985; *Lyzenga*, 1986; *Brüning et al.,* 1988; *Raney and Vachon*, 1988; *Jensen*, 1991]. An important step ahead occurred when *Hasselmann and Hasselmann* [1991] and later *Krogstad* [1992] derived an expression for the non-linear transfer function in the spectral domain. Prior to this development, complete analyses of ocean surface wave imaging had required a Monte Carlo approach in which the forward mapping and its intrinsic non-linearity were modelled exclusively in the image domain [*e.g., Alpers*, 1983; *Brüning et al.*, 1990].

The non-linear spectral transform resembles a Fourier transform of the ocean surface wave spectrum, but the transform kernel depends on spatial position and wavenumber, making it genuinely non-linear. *Krogstad* [1992] discussed the numerical evaluation of this transform and the onset and effects of the non-linearity, such as the onset of an azimuth cut-off. There have been many studies that attempt to relate the observed cut-off to ocean and SAR parameters [*e.g., Vachon et al.*, 1994; *Kerbaol et al.*, 1998]. The spectrum computed from the non-linear transform also has an intrinsic azimuth cut-off, which in many cases fits very well with actual observations [*Hasselmann and Hasselmann*, 1991; *Engen et al.*, 1994; *Krogstad et al.*, 1994].

Inversion is the process of deriving an ocean surface wave spectrum from an observed SAR image spectrum. The non-linear inversion problem is usually formulated as the minimization of a cost function that involves the best guess *a priori* ocean surface wave spectrum, which would usually come from a wave model, the non-linear spectral transform, and

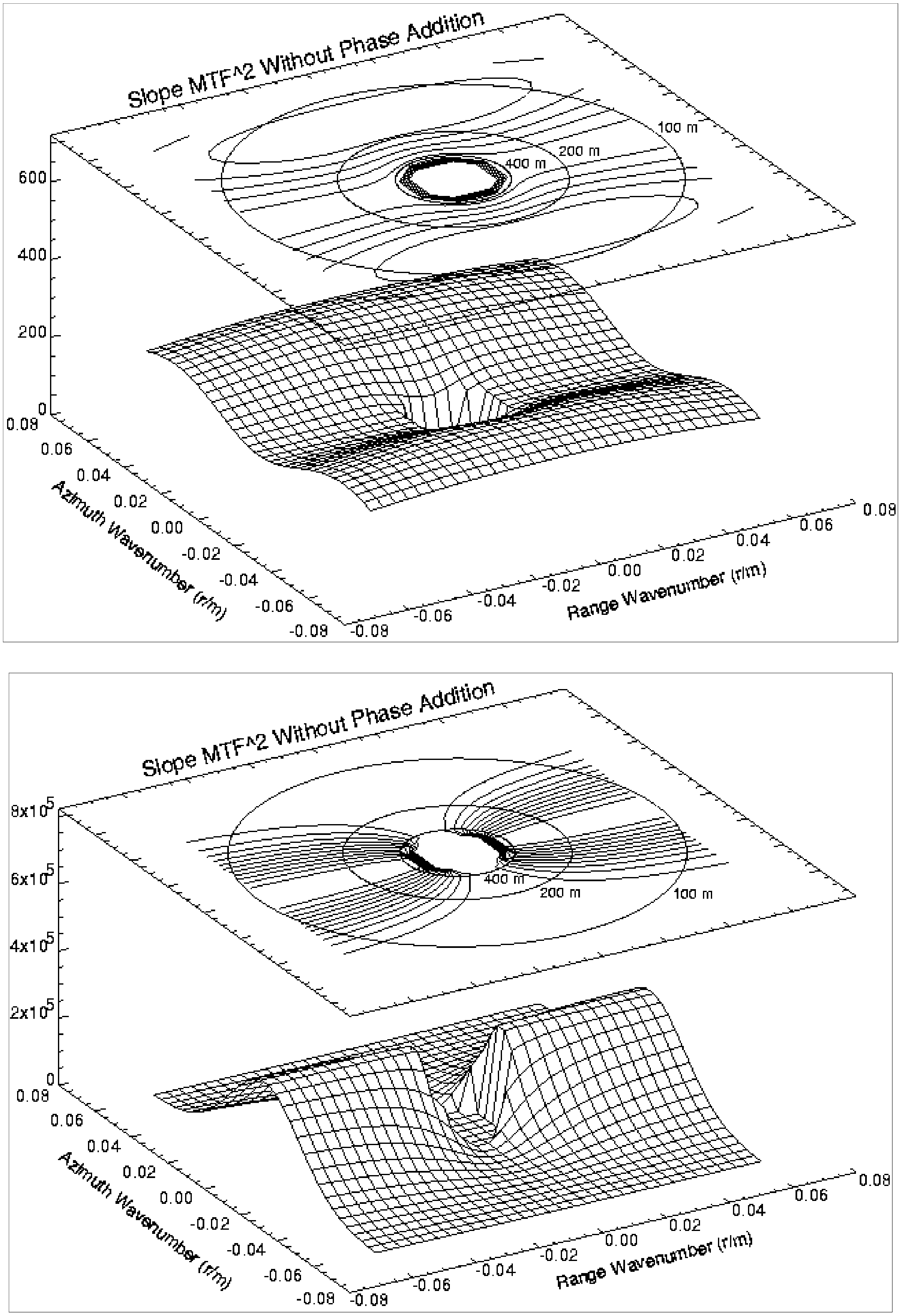

Figure 5.7. SAR transfer function for a) a linear imaging case: $q = 25^\circ$, $\left(R/V\right) = 30$ s, and $H_s = 1$ m and b) a nonlinear imaging case: $q = 25^\circ$, $\left(R/V\right) = 120$ s, and $H_s = 1.6$ m

the observed SAR image spectrum [*Hasselmann and Hasselmann*, 1991]. Weight functions are chosen to identify where in the wavenumber domain the various available spectra apply. For example, no information can be gained directly from the SAR image spectrum from outside of the azimuth passband.

Various choices of the weight functions and other inversion constraints have been considered [*Hasselmann and Hasselmann*, 1991; *Engen et al.*, 1994; *Krogstad et al.*, 1994]. For example, the *a priori* spectrum may be used as a guide in resolving the wave propagation direction and to supply high frequency information for waves that would otherwise be obscured by the azimuth cut-off in the SAR imaging process.

The iterative inversion procedure may be conveniently combined with a quasi-linear approximation to the non-linear spectral transform to produce a fast and simple inversion algorithm [*Krogstad et al.*, 1994]. The fully non-linear ocean-SAR transform may be used for fine-tuning the solution near the end of the iterative procedure. Other *a priori* information, such as the wind vector derived from scatterometery, can also aid the SAR spectral inversion process [*Mastenbroek and de Valk*, 2000]. Recently, *Lyzenga* [2002] described an inversion process that avoids the use of *a priori* information.

5.3.7 Inter-Look Cross Spectrum

A SAR requires a finite period of time, on the order of 1 s for spaceborne systems operating at C-band, to collect the required data to form the synthetic aperture. The waves propagate during this observation interval. An inherent property of large time-bandwidth product systems such as SAR is that there is a one-to-one relationship between Doppler frequency and time. As such, individual looks that are extracted from discrete bands of the Doppler spectrum in order to reduce image speckle, correspond to slightly offset observation times during which the relative position of the imaged wave shifts along the wave propagation direction. Several techniques have been proposed to take advantage of time offset looks in order to resolve the 180° ambiguity in wave propagation direction that is inherent in a single SAR image [*Vachon and Raney*, 1991; *Vachon and West*, 1992].

The most advanced approach, proposed by *Engen and Johnsen* [1995], uses the inter-look image cross spectrum. Phase terms present in the cross spectrum allow the wave direction to be resolved in many cases. In addition, by using individual look data from non-overlapping portions of the Doppler spectrum, the inter-look cross spectrum has the important property of canceling a significant portion of the broadband speckle noise contribution to the SAR image spectrum (*i.e.,* multi-looking is carried out specifically to generate images of the same scene with uncorrelated speckle content).

The time separation between looks is given by:

$$\Delta T = \frac{l\,R}{2V_p V_f}\Delta B \tag{8}$$

where l is the radar wave length, R is the scene range, V_p is the platform velocity, V_f is the footprint velocity, and ΔB is the Doppler bandwidth between look centers. For typical ERS or RADARSAT-1 SAR parameters, the time offset for individual looks corresponds to a few tenths of a second, which is often adequate to resolve the wave propagation direction. As such, there may be less reliance on *a priori* wave information (from models for resolving wave propagation direction ambiguities, for example) when inverting the SAR image spectra. Some of these benefits of inter-look cross spectra are illustrated by the example SAR image spectra that are considered in the next section.

5.4 Applications

5.4.1 Examples of SAR Image Spectra

Figures 5.8a and 5.8b show two examples of SAR images and image spectra derived from contemporaneous ERS-1 and airborne SAR images, along with the corresponding in-situ measured directional ocean surface wave spectrum. The data were acquired during an ERS-1 validation project in late 1991 [see *Dobson and Vachon*, 1994].

For the ERS-1 SAR cases, we have included the conventional image spectrum and the magnitude of the inter-look cross spectrum. Comparison of these two spectra illustrates the reduction in broadband background noise through the reduction of the speckle contribution to the image spectrum. We have also included the directionally resolved image spectrum that arises by keeping only those components of the inter-look cross spectrum that have a negative phase component (corresponding to a "going-to" wave propagation direction convention).

Airborne SAR image spectra that were acquired at the same time and location are also available. The airborne SAR data were acquired with a small (R/V) compared to the spaceborne SAR data, which is strikingly evident by comparing the degree of azimuthal cut-off. The airborne SAR spectra contain much more information in azimuth, illustrating the fundamental geometry constraint of polar orbiting spaceborne SARs.

The corresponding in-situ directional spectrum was measured by a moored buoy and was transformed into directional wavenumber format. For the 18 November 1991 case (Figure 5.8a) a long swell was present and it is clear from the images and the respective image spectra that the two SARs have measured the same ocean surface wave component as the buoy. For the 23 November 1991 case (Figure 5.8b) the situation was more dynamic with both a swell and developing wind sea present. It is evident that the SAR has significantly shifted the wavelength and apparent propagation direction of the shorter wave mode towards range travelling direction due to the non-linear nature of velocity bunching causing an azimuth cut-off. Also apparent from the image are cells of several kilometers scale that are aligned with the wind direction, which are SAR image signatures of convection.

To better illustrate the azimuth cut-off effect, Figure 5.8c shows the azimuth spectra corresponding to these two sets of spectra. In effect, the Look Sum spectrum and the two Cross Spectra from each case were integrated in the range wavenumber direction and plotted relative to the local spectral maximum. In each case, for ERS-1, we see more than an 8 dB reduction in the speckle noise in comparing the Look Sum spectrum to the magnitude of the cross spectrum. Also evident is the broader azimuth passband for the CV-580 spectra, acquired in each case with a much smaller R/V than that of ERS-1.

5.4.2 Wave Refraction

Several studies have used SAR to observe wave refraction related to bathymetry, propagation through sea ice (see below) [*Liu et al.*, 1991B] and through a current field as an indirect means of deriving current velocity [*Beal et al.*, 1983, 1986; *Barnett et al.*, 1989]. Ray tracing has often been used to model the current and resulting wave refraction to compare with

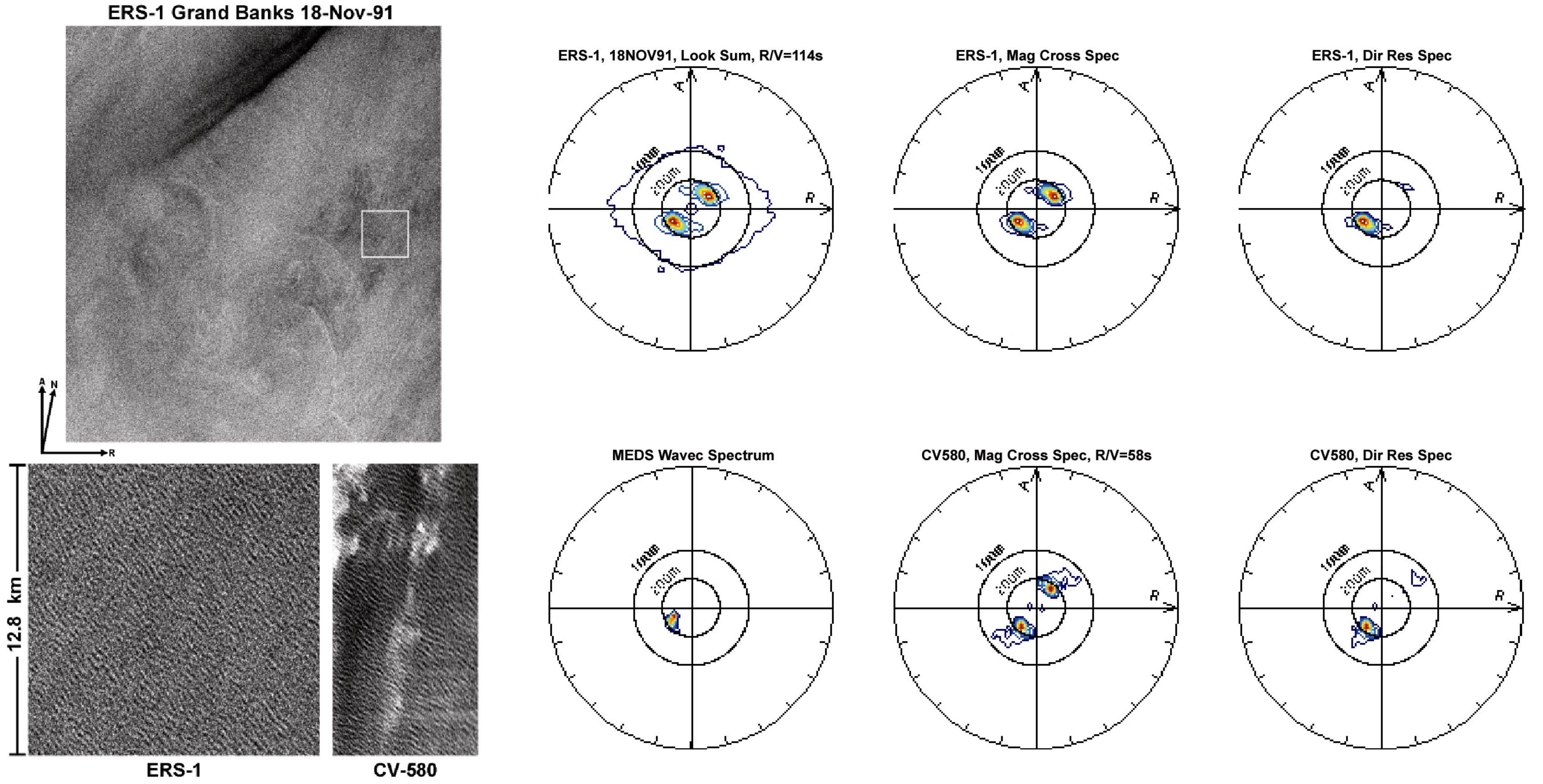

Figure 5.8a. Example SAR image spectra from the ERS-1 (C-band, VV) and CV-580 (C-band, HH) SARs and the corresponding in-situ ocean wave spectrum (lower-left) acquired during an ERS-1 SAR validation field program carried out on the Grand Banks of Newfoundland in November 1991. The measured wind speed was 10 m s^{-1} and the wave height was 3.4 m. This case is dominated by swell and there appears to be general agreement among the SARs and the wave buoy in terms of the direction and length of the dominant spectral peak. Included are the ERS-1 Look Sum image spectrum (upper-left), as well as the magnitude (center column) and directionally resolved (right-hand column) spectra derived from individual look image data of the inter-look cross spectrum for both SARs.

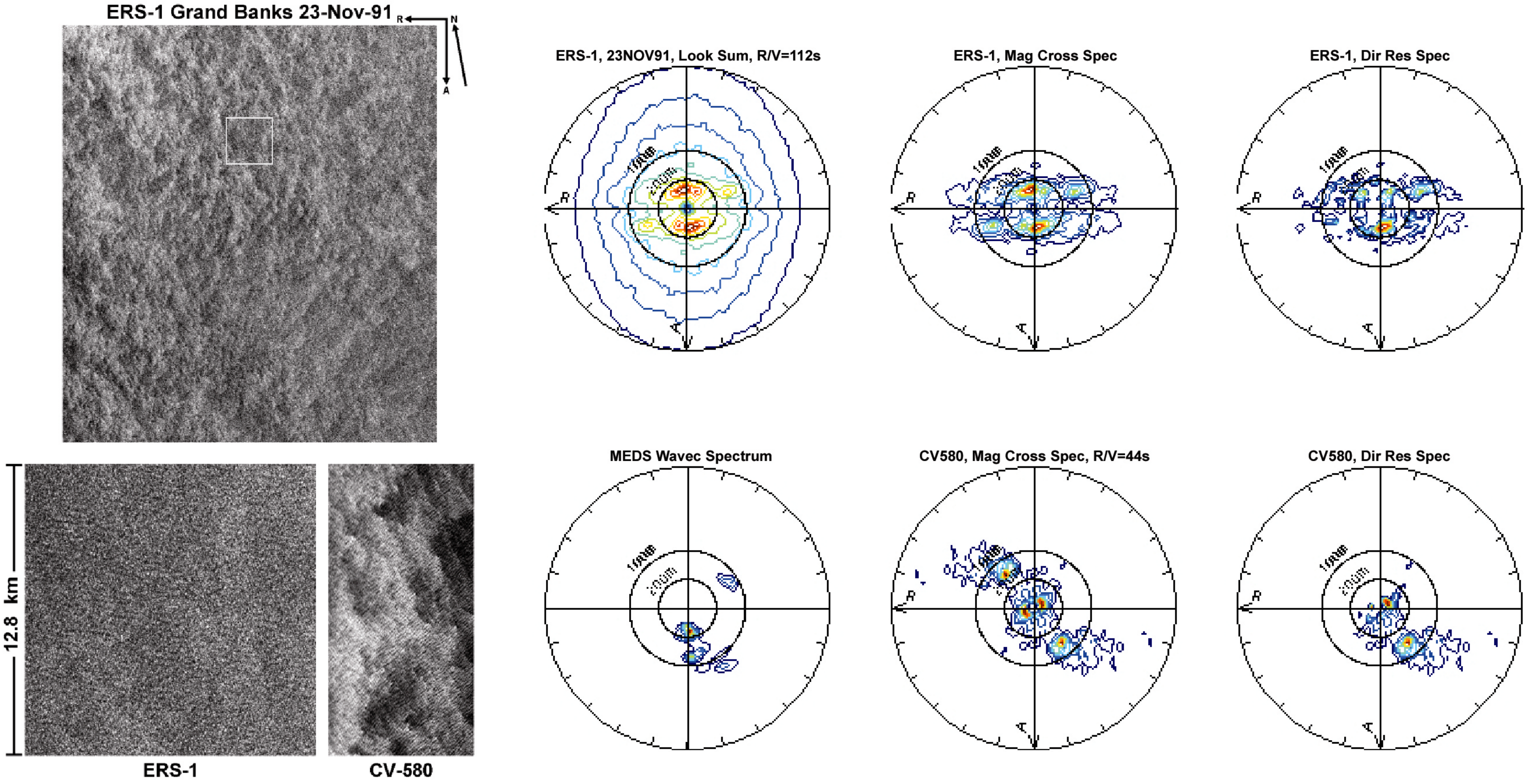

Figure 5.8b. As for Figure 5.8a, but acquired on 23 November 1991. In this case, the measured wind speed was 8 m s^{-1} and the wave height was 3.7 m. The ERS-1 image spectrum is severely constrained in the azimuth direction compared to the CV-580 image spectrum. This is also apparent from inspection of the respective SAR images. According to the wave buoy, several wave modes were present.

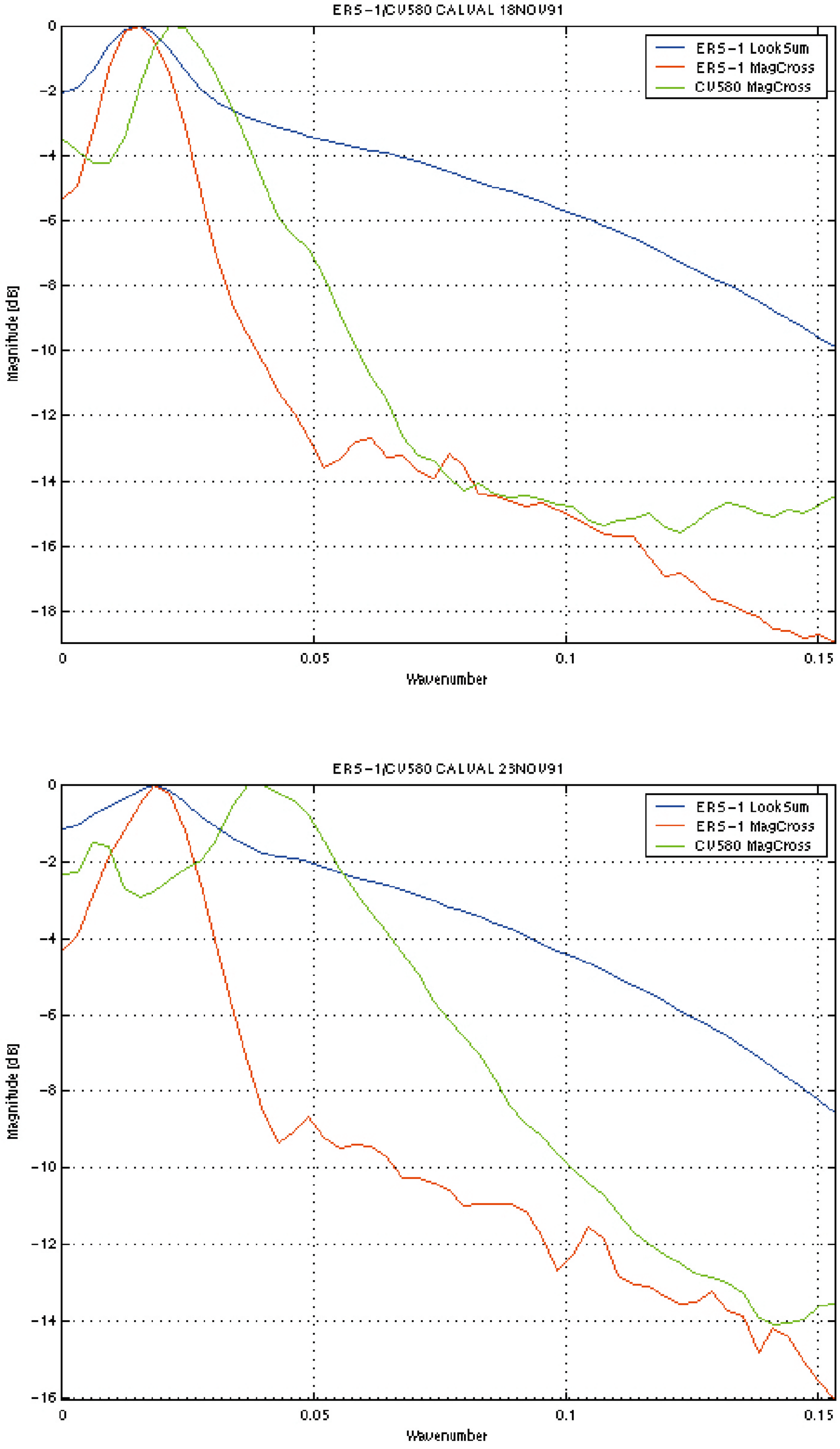

Figure 5.8c. Azimuth image spectra for the cases of Figure 5.8a (top) and 5.8b (bottom).

the SAR measurements [*e.g., Liu et al.*, 1989; *Irvine and Tilley*, 1988]. *Liu et al.* [1994] used ray tracing to detect eddies in SAR imagery by assuming that the propagating long swells of interest were imaged in a linear manner. As such, the evolution of the peak location in the SAR image spectrum was correlated directly with predictions from a ray-tracing model.

5.4.3 Waves in Ice

In the polar regions, ocean surface waves interact with the sea ice cover in several geophysically important ways [see *Squire et al.*, 1995; *Wadhams*, 2000]. Waves can alter the morphology and distribution of the ice cover. Incoming waves may cause an effectively continuous ice cover to flex and break into smaller floes. Floe-floe interaction from waves increases floe deformation, especially around the edges. The newly fractured ice cover becomes even more responsive to redistribution by winds and underlying currents and to melting through increased contact with the relatively warmer ocean. A persistent swell can then lead to the rapid disintegration and reduction of an extensive marginal ice zone [*Carsey et al.*, 1989]. In other regions, particularly surrounding Antarctica, considerable ice formation takes place in turbulent conditions at the outermost margins of the ice cover. The ice forms as a viscous slurry of so-called frazil crystals, which gradually accrete into small (1 m to 3 m) diameter floes, called pancake ice. Extensive zones may be composed of pancake ice, as the incoming swell serves to maintain pancake edge abrasion while also preventing the loose pancakes from forming into consolidated pancakes. The heat transfer from the ocean to the air is greater for pancake ice than thicker ice types.

Conversely, the highly varying ice cover may damp incoming waves. Wave attenuation, or reduction of energy, increases with increasing penetration into the ice cover, with the attenuation coefficient generally decreasing with increasing wave period. The dispersion relation may be altered compared to the open water, depending on whether the ice cover is composed of frazil/pancakes/small floes or is a more continuous and elastic ice cover made up of interacting larger floes. Wave refraction and reflection also take place. Thus waves can be used as a diagnostic tool for ice properties and mechanics.

SAR observations of ocean surface waves propagating into the marginal ice zone (MIZ) have been used to address two main research objectives: first, to provide a synoptic-scale overview for the study of wave evolution in the sea ice cover (discussed further below); and second, to work towards an understanding of the SAR imaging physics for ocean surface waves by studying the simplified case (for SAR) of waves-in-ice [*Lyzenga et al.*, 1985; *Vachon et al.*, 1993].

For waves-in-ice, the ice cover acts as a natural low-pass filter, essentially eliminating the high frequency waves. This has two effects for the SAR: first, the SAR no longer relies upon Bragg scattering from time-dependent patches on the ocean surface; and second, the effective scene coherence time is lengthened so that the degree of azimuth cut-off is reduced. The ice cover also inhibits hydrodynamic modulation of radar cross-section in terms of wave-wave interactions modifying the Bragg-scale waves. Thus, the case of waves-in-ice allows direct observation of the velocity bunching SAR imaging mechanism. Waves within the ice are often more clearly detected on SAR imagery than the same wave field before it enters the ice cover.

Wave attenuation measurements in the marginal ice zone from airborne SAR imagery off the Labrador coast were found to favorably compare with a wave-ice model [*Liu et al.*, 1991a; 1992]. The attenuation measurements were derived from the contrast in the spectral peak, which is analogous to wave amplitude. Other studies used the SAR spectral measurements to estimate

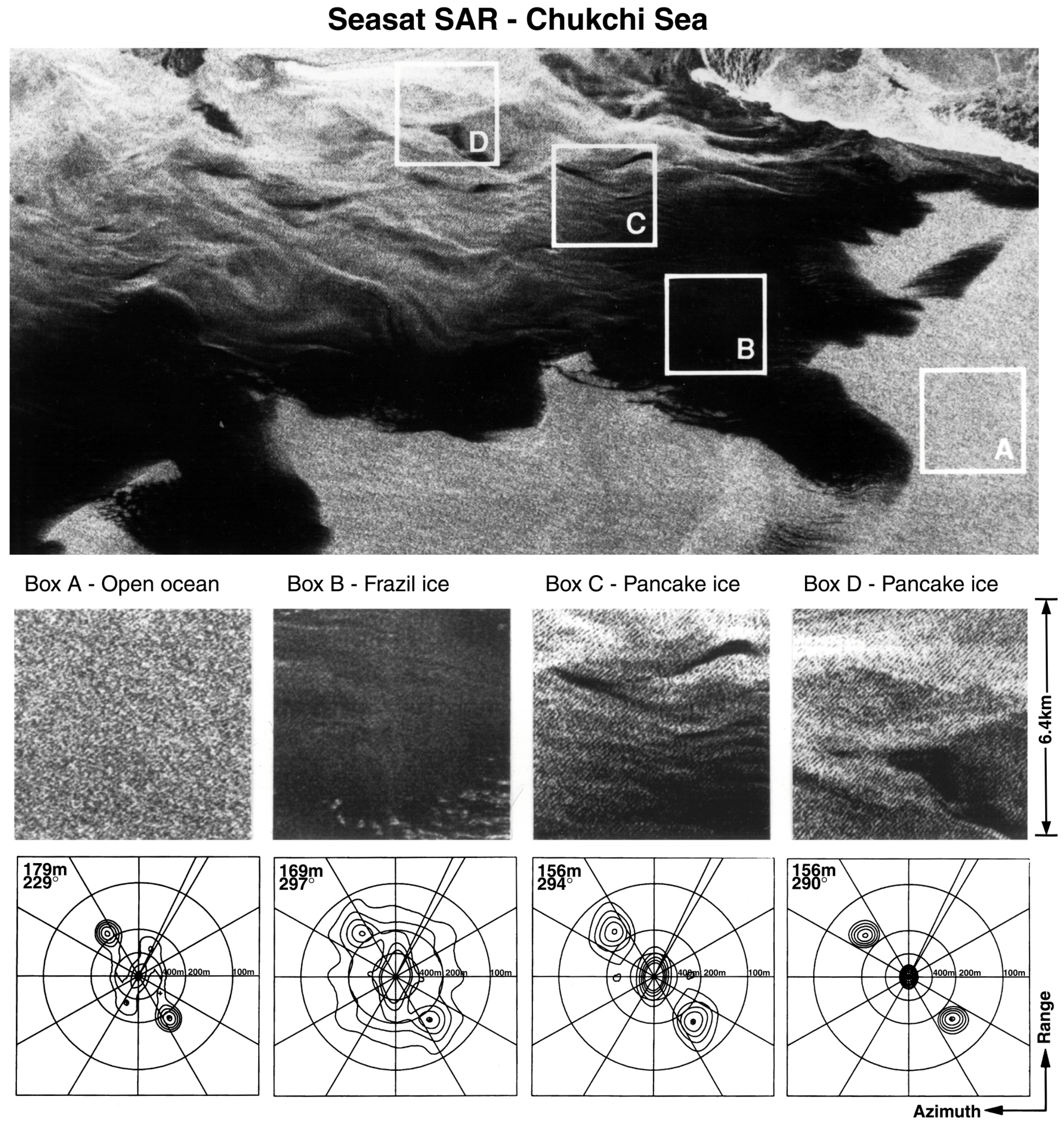

Figure 5.9. SEASAT (L-band, HH) SAR image of the Chukchi Sea acquired 8 October 1978 and associated wave spectra. Boxes A through D are enlargements from areas shown on top image and associated wave spectra (below), labeled as open water (A), frazil ice (B), and pancake ice (C-D). Note the reduction in appearance of waves in Box B, as frazil ice dampens out shorter frequency waves and hence reduces Bragg scattering. The incoming waves are shortened in wavelength and show slight refraction due to wave attenuation imparted by the ice cover. [After *Wadhams and Holt*, 1991].

ice thickness, based on comparisons with theoretical estimates of wave dispersion in different ice types and models [*Wadhams and Holt*, 1991; *Shuchman et al.*, 1994]. Figure 5.9 illustrates attenuation and refraction of waves passing through frazil and pancake ice on SEASAT SAR imagery. Note the reduction in spectral noise as higher frequency wave components are damped [*Wadhams and Holt*, 1991; *Shuchman et al.*, 1994]. Figure 5.9 illustrates attenuation and

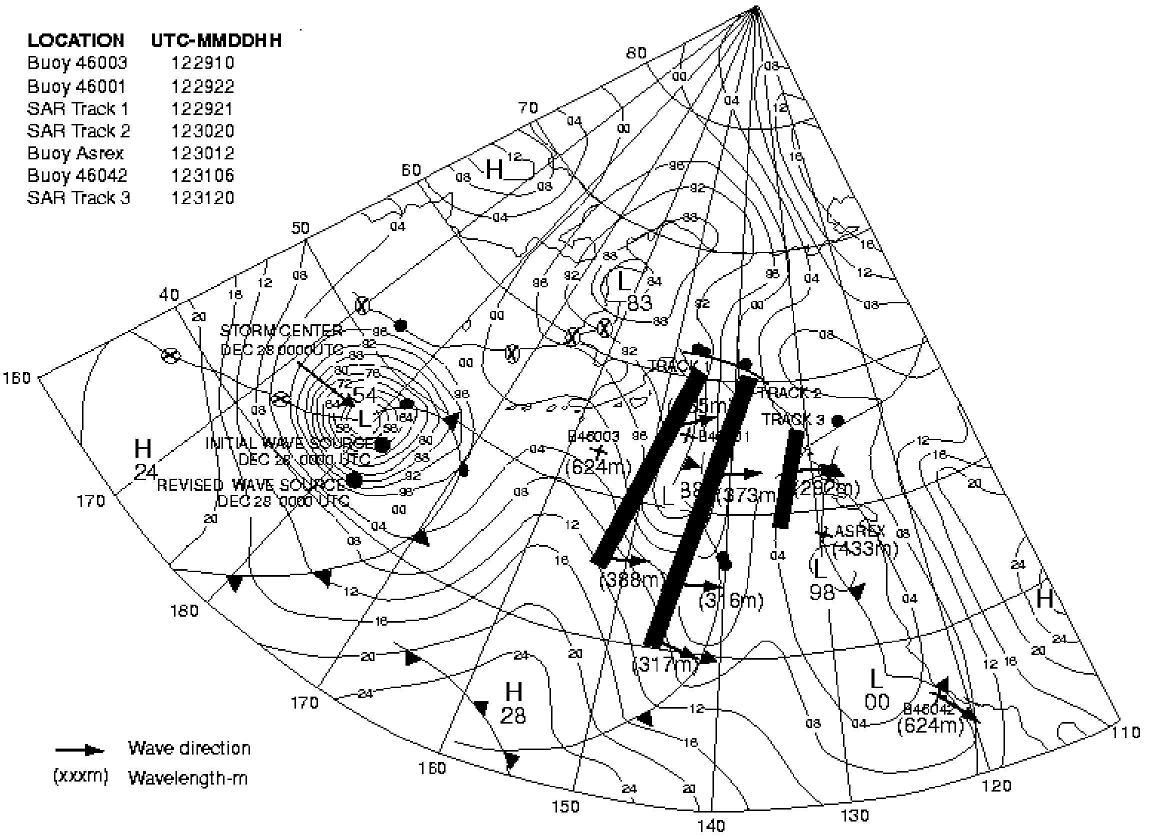

Figure 5.10. Schematic of storm-generated waves in the Pacific Ocean from 1991, showing the location and times of wave buoys and ERS-1 SAR measurements from 3 acquisition tracks. Wavelength and wave direction (where available) are indicated. Superimposed is the surface analysis synoptic weather chart at 0000 UTC on 28 December 1991 from the National Climatic Data Center. The low pressure region (954 mbar) identifies the storm location. Also shown are the initial and revised wave source regions. [After *Holt et al.,* 1998.]

refraction of waves passing through frazil and pancake ice on SEASAT SAR imagery. Note the reduction in spectral noise as higher frequency wave components are damped as the waves pass through frazil ice and into pancake ice. Additional studies examined the impact of waves on the ice edge and water/ice edge upper circulation [*Liu et al.*, 1991b; 1993; 1994). Interestingly, for nearly all of these SAR studies, while the SAR measurements appear accurate, the wave-ice models developed to explain the SAR measurements have encountered controversy [*Squire et al.*, 1995; *Squire*, 1995; *Newyear and Martin*, 1999]. Lastly, a recent study using ERS-1 SAR imagery made use of the inter-look cross spectra technique to assess waves traveling through frazil and pancake ice [*De Carolis*, 2001].

5.4.4 Storm-Generated Wave Fields

Waves generated by storms have been examined with SAR imagery both near to and far from the source regions. Such studies provide insight to the characteristics and variability of large storms and how energy is transmitted into the upper ocean, and improve predictive capabilities for monitoring potentially hazardous conditions for ship navigation and coastal hazards.

Within the close proximity of hurricanes, multiple fan-shaped wave fields of varying energy have been identified as emanating from the rotating wind fields, using aircraft [*e.g., Elachi et al.*, 1977], SEASAT [*Gonzalez et al.*, 1982; *McLeish and Ross*, 1983], and SIR-B imagery [*Holt and Gonzalez*, 1986; *Gonzalez et al.*, 1987; *Monaldo et al.*, 1993]. The large H_s within hurricanes forces the azimuth cut-off toward longer wavelengths (Equation 6). However, for the SIR-B imagery of Hurricane Josephine, the lower platform altitude resulted in a small R/V and a lower degree of azimuth cut-off. One study estimated the age of the waves (between 0 and 9 hours) as well as radial distance (between 200 km and 300 km) of generation from Josephine's center [*Gonzalez et al.*, 1987]. Making use of the fact that the dominant wave field of Josephine rotated over 90°, *Monaldo et al.* [1993] examined the effect of three different wave imaging mechanisms on the SAR modulation transfer function.

Early oceanographic studies found that swell can propagate large distances from their generation source [*e.g., Barber and Ursell*, 1948; *Munk et al.*, 1963]. Using SEASAT SAR imagery, *Beal et al.* [1986] examined the spatial evolution of a storm-generated wave field that propagated northward across the North Atlantic and through the Gulf Stream. In that case, different dominant wave fields had been generated from different times and stages of the highly variable tropical depression. Two more recent studies have compared ERS-1 SAR wave spectra with wave model hind casts, followed by the use of simple kinematic models to retrace the waves over considerable distances to the source region [*Holt et al.*, 1998; *Heimbach and Hasselmann*, 2000]. In both cases, the source regions were recalculated based on the SAR spectra and by invoking the deep-water group velocity, $C_g = \frac{1}{2}\sqrt{g/k}$. In one case, the recalculated source region was considerably farther away from the storm center than the initial estimate for the radius of maximum winds [*Holt et al.*, 1998] (Figure 5.10). Using this revised position, the recalculated wave travel times were found to match more closely with the remote buoy records than in the original comparisons. This suggested the value of using SAR directional wave spectral information for advanced warning of high swell, which could be critical to the safety of offshore operations and coastal regions.

5.4.5 Real-Time Wave Demonstration

The SIR missions with their low values of R/V demonstrated significantly improved response to azimuth-traveling waves [*Monaldo and Lyzenga*, 1986; 1988; *Monaldo et al.*, 1993]. As a demonstration of the benefits of this approach, the Johns Hopkins University, Applied Physics Laboratory designed and built an onboard processor that was carried on the space shuttle *Endeavour* during the SIR-C mission. Raw C-band SAR signal data were sent to a processor that computed 7.68 km × 7.68 km, 30-m resolution images, and computed the image spectra in real time. An image spectrum was sent to the ground every 1.3 s. SAR image spectra were then computed and relayed back to earth in real-time, and were posted on the World Wide Web [*Monaldo and Beal*, 1995; 1998]. During the two SIR-C missions, over 100,000 SAR image spectra were computed, mapping the Southern Ocean surface wave field. Figure 5.11 shows two spectra from orbit crossovers separated by six hours. The image spectra were computed in real time during the SIR-C mission. The spectra were converted to slope-variance and show nearly the same ocean surface wave spectra from two different aspect angles; nearly the same result is achieved in each case. This example clearly demonstrates that by choosing the SAR geometry to reduce R/V, it is possible to accurately image waves with high fidelity, whether they are traveling in the range or azimuth directions.

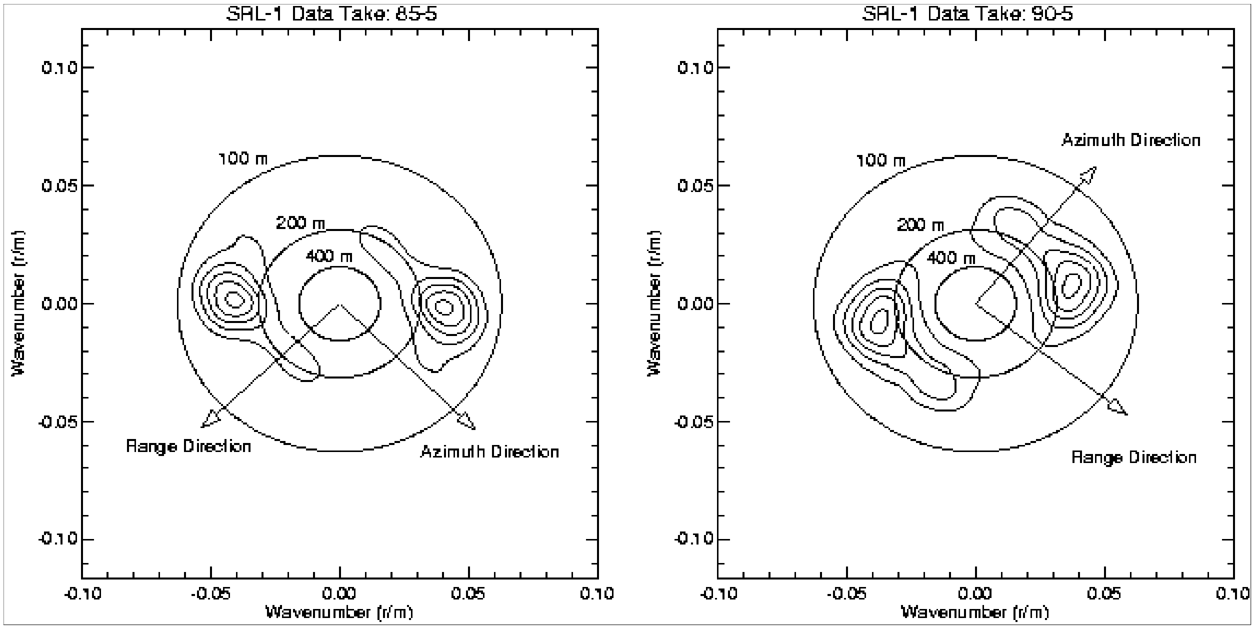

Figure 5.11. Wave height variance spectra from the Southern Ocean derived from SAR image spectra that were acquired and processed by the SIR-C onboard wave processor in near-real time.

5.4.6 Wave Groups from SAR Imagettes

Wind generated waves tend to form well-defined wave groups that travel across the ocean. Wave groups, characterized by sequences of high waves with nearly equal wave lengths, can cause serious damage to ships, as well as to on- and offshore structures, especially when the period of the individual waves in the group is close to the resonance period of the ship or structure. Furthermore, wave groups can contain extremely large wave heights, which increase the danger to offshore activities.

Traditionally, studies of wave groups have been based upon wave elevation time series measured by buoys anchored at fixed ocean locations. A common method to analyze wave groups from wave elevation time series is based on estimation of the statistical properties of runs. A run is a set of consecutive waves with wave heights higher than a specified threshold height. Typically, the threshold heights may be the median wave height or the significant wave height [*Goda*, 1995].

At present, global satellite data can provide information on single waves and wave groups. For more than a decade, the ERS-1/2 satellites have almost continuously recorded SAR imagettes of the ocean surface. Operating in wave mode, these instruments have acquired roughly 1400 imagettes per day (10 km by 5 km in size, spaced every 200 km along the orbit). The accumulated database permits the study of ocean surface wave properties on a global basis [see *Lehner et al.*, 2000].

Unfortunately, only coarsely gridded SAR image spectra are available as official wave mode products from ESA. Improved processing methods have been developed since the initial availability of ERS-1 wave mode data. As a demonstration, about three weeks of ERS-2 SAR wave mode raw data were reprocessed to provide 34,000 complex SAR images using the BSAR processor of the German Aerospace Center (DLR). Note that ENVISAT will provide almost 3000 imagettes per day with its higher along-track sampling rate (spaced every 100 km).

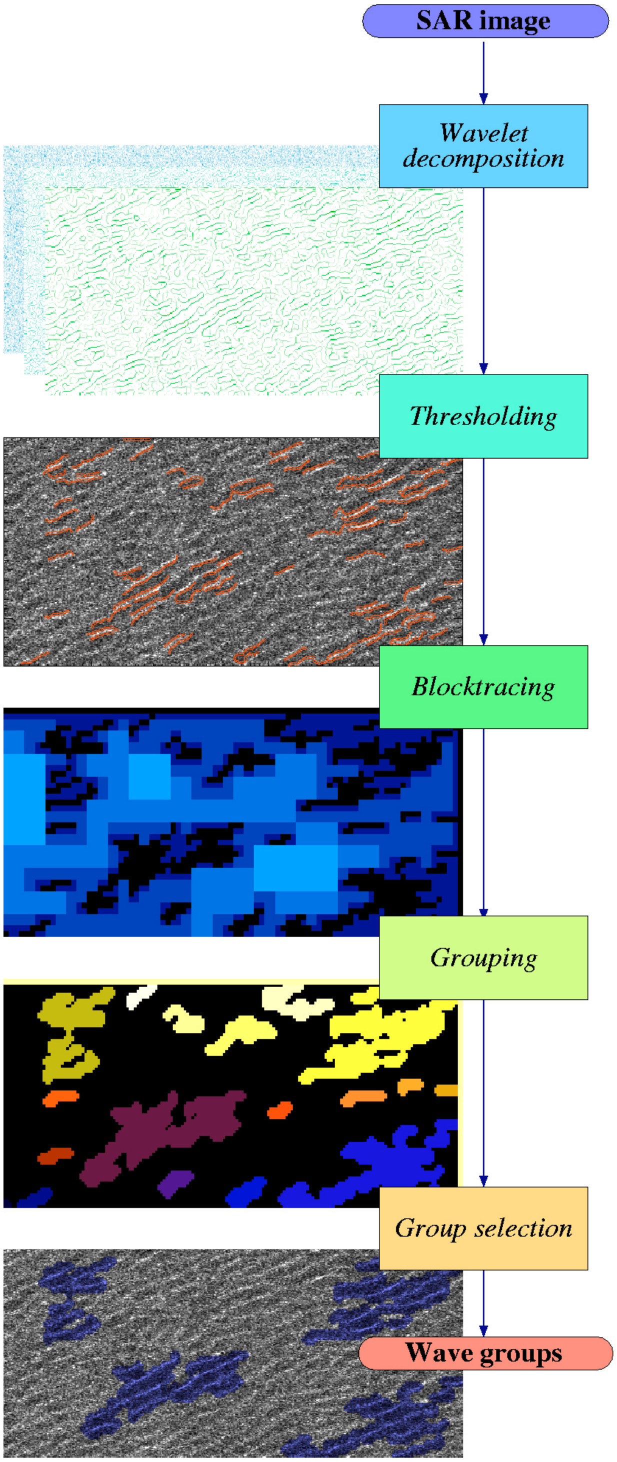

Figure 5.12. The Grouping Algorithm applied to an ERS-2 SAR imagette acquired on 7 October 1996, 0732 UTC at 61°11'S 22°47'E; $H_s >> 3.4$ m, $\Lambda = 238$ m. This imagette is part of the data set that was reprocessed at the German Aerospace Center, DLR.

By applying a wavelet-based edge detection method to the amplitude imagettes and using a region-growing algorithm to encompass edge free areas, it is possible to estimate the group run size and the number of large groups as measures of wave "groupiness" in each imagette. The wavelet coefficients provide a measure of edge strength that is correlated to both wave height and steepness. Thus, groups of waves that are higher and steeper than the surrounding sea surface may be found and isolated.

Figure 5.12 provides an overview of this wave grouping algorithm applied to an ERS-2 SAR imagette. The edge detection (decomposition and thresholding) and block tracing are described by *Niedermeier et al.* [2002]. Wavelet edge detection applied to range travelling ocean surface waves provides edge positions that approximately fit the position of the actual wave crests and valleys on the ocean surface. Block tracing separates regions with high and low edge density and is used for wave group separation. Grouping then enumerates the disjoint groups and selects those above a certain area threshold to yield the large groups that are delineated on the imagette.

Using this data set and these techniques, a global map of dangerous areas (high wave group activity) may be generated. This information will help to avoid ship accidents caused by severe weather conditions in dangerous areas. Many of the ships lost in such cases report damage due to groups of several high waves (*i.e.*, three sisters).

5.5 Future Prospects

For continuity with the ERS missions, ESA launched ENVISAT in early 2002. ENVISAT carries an Advanced SAR (ASAR) that features single beam modes, dual-polarization modes, ScanSAR, as well as an improved wave mode. The latter will provide imagettes with more acquisition choices (*e.g.,* geometry, along track spacing, and polarization). Furthermore, the distributed products will be based upon the inter-look cross spectrum technique and will feature all of the benefits of that method. Beyond this, ESA will provide methodology to invert the ENVISAT wave mode products into ocean surface wave spectra. The single beam mode will offer dual polarization acquisition, which could provide important opportunities to better understand the RAR modulation transfer function by using methods such as those of *Engen et al.* [2000].

Future satellites that will carry SAR include the Japanese ALOS and RADARSAT-2. ALOS will carry an L-band SAR, while RADARSAT-2 will carry a C-band SAR. Both will offer fully polarimetric modes of acquisition, which could provide further insight into SAR ocean surface wave imaging. All of these future missions will be polar orbiting, which does not offer an optimal SAR geometry for ocean surface wave imaging.

Nevertheless, the understanding of the SAR wave imaging process has reached a point where use of the now extensive SAR image catalogues of surface waves, particularly from the over ten years of data from the two ERS missions and over 5 years from RADARSAT-1, can be examined with considerable confidence. These data sets may be considered for climate studies. For example, *Young* [1999] assessed ten years of satellite data to determine the seasonal variability of wind and waves. For wave period and direction, this analysis used model results from a third generation spectral global wave model (WAM) rather than ERS SAR imagery because the transfer function between the SAR and wave spectrums was thought to not be conclusive. More recently, comparisons of ERS SAR wave mode data and WAM found WAM to over predict wind-sea wave heights and under predict swell wave heights [*Heimbach and Hasselmann*, 2000]. Furthermore, several studies are finding climatically related changes in wave height and winds, reflecting changes in storm intensities due to oscillating atmospheric patterns [*Kushnir et al.*, 1997; *Gulev and Hasse*, 1999; *Young*, 1999; *Allan and Komar*, 2000]. This suggests there is much remaining to be learned from these extensive SAR ocean surface wave data sets, including improvements to wave models and the impacts of climate change and subsequent effects on coastal hazards.

5.6 References

Allan, J., and P. Komar, 2000: Are ocean surface wave heights increasing in the eastern North Pacific? *Eos Trans. Amer. Geophys. Union,* **81**, 566–567.

Alpers, W. R., 1983: Monte Carlo simulations for studying the relationship between ocean surface wave and synthetic aperture radar image spectra. *J. Geophys. Res.,* **88***,* 1745–1759.

——, and C. L. Rufenach, 1979: The effect of orbital velocity motions on synthetic aperture imagery ocean surface waves. *IEEE Trans. Antennas Propag.,* **27**, 685–690.

——, and C. Brüning, 1986: On the relative importance of motion-related contributions to the SAR imaging mechanism of ocean surface waves. *IEEE Trans. Geosci. Remote Sens.,* **24**, 873–885.

——, D. B. Ross, and C. L. Rufenach, 1981: The detectability of ocean surface waves by real and synthetic aperture radar. *J. Geophys. Res.,* **86**, 6481–6498.

——, C. Brüning, and K. Richter, 1986: Comparison of simulated and measured synthetic aperture radar image spectra with buoy-derived ocean surface wave spectra during the shuttle imaging radar-B mission. *IEEE Trans. Geosci. Remote Sens.,* **24**, 559–566.

Barber, N. F., and F. Ursell, 1948: The generation and propagation of ocean surface waves and swell. *Philos. Trans. Roy. Soc. London,* **240A**, 527–560.

Barnett, T. P., F. Kelley, and B. Holt, 1989: Estimation of the two-dimensional ocean current shear field with a synthetic aperture radar. *J. Geophys. Res.,* **94** (C11), 16 087–16 095.

Beal, R. C., 1980: Spaceborne imaging radar: Ocean surface wave monitoring. *Science,* **208***,* 1371–1375.

——, P. S. DeLeonibus, and I. Katz, Ed., 1981: *Spaceborne Synthetic Aperture Radar for Oceanography*. Johns Hopkins University Press, 215 pp.

——, D. G. Tilley, and F. M. Monaldo, 1983: Large- and small-scale spatial evolution of digitally processed ocean surface wave spectra from the Seasat synthetic aperture radar. *J. Geophys. Res.,* **88***,* 1761–1778.

——, T. W. Gerling, D. E. Irvine, F. M. Monaldo, and D. G. Tilley, 1986: Spatial variations of ocean surface wave directional spectra. *J. Geophys. Res.,* **91** (C2), 2433–2449.

Borgman, L. E., 1982: Summary of the probability laws for wave properties. *1980 Proceedings of the International School of Physics "Enrico Fermi,"* A. R. Osborne and P. M. Rizzoli, Eds., North Holland Publishing, 373–386.

Breivik, L.-A., M. Reistad, H. Schyberg, J. Sunde, H. E. Krogstad, and H. Johnsen, 1998: Assimilation of ERS SAR wave spectra in an operational wave model. *J. Geophys. Res.,* **103** (C4), 7887–7900.

Brüning, C., W. R. Alpers, and L. Zambresky, 1998: Validation of synthetic aperture radar ocean surface wave imaging theory by the shuttle imaging radar-B experiment over the North Sea. *J. Geophys. Res.,* **93**, 10 403–10 425.

——, ——, and K. Hasselmann, 1990: Monte-Carlo simulation studies of the non-linear imaging of a two dimensional surface wave field by a synthetic aperture radar. *Int. J. Remote Sens.,* **11***,* 1695–1727.

Carsey, F. D., S. A. Digby Argus, M. J. Collins, B. Holt, C. E. Livingstone, and C. L. Tang, 1989: Overview of LIMEX'87 ice observations. *IEEE Trans. Geosci. Remote Sens.,* **27**, 468–482.

De Carolis, G., 2001: Retrieval of the ocean surface wave spectrum in open and thin ice covered ocean waters from ERS synthetic aperture radar images. *Il Nuovo Cimento,* **24**, 53–66.

Dobson, F. W., and P. W. Vachon, 1994: The Grand Banks ERS-1 SAR wave spectra validation experiment: Program overview and data summar. *Atmos.–Ocean,* **32**, 7–29.

Dowd, M., P. W. Vachon, F. W. Dobson, and R. B. Olsen, 2001: Ocean surface wave extraction from RADARSAT synthetic aperture radar inter-look image spectra. *IEEE Trans. Geosci. Remote Sens*., **39**, 21–37.

Dunlap, E. M., R. B. Olsen, L. Wilson, S. De Margerie, and R. Lalbeharry, 1998: The effect of assimilating ERS-1 fast delivery wave data into the North Atlantic WAM model. *J. Geophys. Res.,* **103** (C4), 7901–7916.

Elachi, C., and W. E. Brown Jr., 1977: Models of radar imaging of the ocean surface. *IEEE Trans. Antennas Propag.,* **25**, 84–95.

——, T. W. Thompson, and D. King, 1977: Ocean surface wave patterns under Hurricane Gloria: Observations with an airborne synthetic aperture radar. *Science,* **198**, 609–610.

Engen, G., and H. Johnsen, 1995: SAR-ocean wave inversion using image cross spectra. *IEEE Trans. Geosci. Remote Sens.,* **33**, 1047–1056.

——, ——, and H. E. Krogstad, 1994: Directional wave spectra by inversion of ERS-1 synthetic aperture radar ocean imagery. *IEEE Trans. Geosci. Remote Sens.,* **32**, 340–352.

——, P. W. Vachon, H. Johnsen, and F. W. Dobson, 2000: Retrieval of ocean surface wave spectra and RAR MTFs from dual-polarization SAR data. *IEEE Trans. Geosci. Remote Sens.,* **38**, 391–403.

Fu, L.-L., and B. Holt, 1982: Seasat views oceans and sea ice with synthetic-aperture radar. Jet Propulsion Laboratory JPL Publication 81-120, Pasadena, CA, 200 pp.

Goda, Y., 1995: *Random Seas and Design of Maritime Structures*. University of Tokyo Press, 323 pp.

Goldfinger, A. D., 1982: Estimation of spectra from speckled image. *IEEE Trans. Geosci. Remote Sens.,* **24**, 675–681.

Gonzalez, F. I., and Coauthors, 1980: Seasat synthetic aperture radar: Ocean surface wave detection capabilities. *Science,* **204***,* 1418–1421.

——, T. W. Thompson, W. E. Brown Jr., and D. E. Weissman, 1982: Seasat wind and wave observations of northeast Pacific Hurricane Iva, August 13, 1978. *J. Geophys. Res.,* **87** (C5), 3431–3438.

——, B. Holt, and D. G. Tilley, 1987: The age and source of ocean swell observed in Hurricane Josephine. *Johns Hopkins APL Tech. Dig.,* **8**, 94–99.

Gulev, S. K., and L. Hasse, 1999: Changes of wind waves in the North Atlantic over the last 30 years. *Int. J. Climatol.,* **19**, 1091–1117.

Harger, R. O., 1970: *Synthetic Aperture Radar Systems*. Academic Press, 240 pp.

Hasselmann, K., and S. Hasselmann, 1991: On the nonlinear mapping of an ocean surface wave spectrum into a synthetic aperture radar image spectra. *J. Geophys. Res.,* **96***,* 10 713–10 729.

——, and Coauthors*,* 1985: Theory of synthetic aperture radar imaging of ocean surface waves: A MARSEN view. *J. Geophys. Res.,* **90***,* 4569–4686.

——, S. Hasselmann, C. Brüning, and A. Speidel, 1991: Interpretation and application of SAR wave image spectra in wave models. *Directional Ocean Surface Wave Spectra,* R. C. Beal, Ed., Johns Hopkins University Press, 117–124.

Heimbach, P., and K. Hasselmann, 2000: Development and application of satellite retrievals of ocean surface wave spectra. *Satellites, Oceanography and Society*, D. Halpern, Ed., Elsevier Science, 5–33.

——, S. Hasselmann, and K. Hasselemann, 1998: Statistical analysis and intercomparison of WAM model data with global ERS-1 SAR wave mode spectral retrievals over 3 years. *J. Geophys. Res.,* **103** (C4), 7931–7977.

Holt, B., and F. I. Gonzalez, 1996: SIR-B observations of dominant ocean surface waves near Hurricane Josephine. *J. Geophys. Res.,* **91**, 8595–8598.

——, A. K. Liu, D. W. Wang, A. Gnanadesikan, and H. S. Chen, 1998: Tacking storm-generated waves in the northeast Pacific Ocean with ERS-1 synthetic aperture radar imagery and buoys. *J. Geophys. Res.,* **103** (C4), 7917–7930.

Irvine, D. E., and D. G. Tilley, 1988: Ocean surface wave directional spectra and wave-current interaction from the Shuttle Imaging Radar-B synthetic aperture radar. *J. Geophys. Res.,* **93** (C12), 15 389–15 401.

Jensen, J. R., 1991: The Fourier transform and the power spectral density of SAR imagery of the ocean surface. *Proc. 1991 International Geoscience and Remote Sensing Symposium*, Espoo, Finland, IEEE, 447–450.

Kerbaol, V., B. Chapron, and P. W. Vachon, 1998: Analysis of ERS-1/2 SAR wave mode imagettes. *J. Geophys. Res.*, **103** (C4), 7833–7846.

Krogstad, H. E., 1992: A simple derivation of Hasselmann's nonlinear ocean-SAR transform. *J. Geophys. Res.,* **97** (C2), 2421–2425.

——, O. Samset, and P. W. Vachon, 1994: Generalization of the nonlinear ocean SAR transform and a simplified SAR inversion algorithm. *Atmos.–Ocean,* **32**, 61−82.

Kushnir, Y., V. J. Cardone, and J. G. Greenwood, 1997: The recent increases in North Atlantic wave heights. *J. Climate,* **10**, 2107–2113.

Lehner, S., J. Schulz-Stellenfleth, B. Schättler, H. Breit, and J. Horstmann, 2000: Wind and wave measurements using complex ERS-2 wave mode data. *IEEE Trans. Geosci. Remote Sens.*, **38**, 2246-2257.

Liu, A. K., F. C. Jackson, E. J. Walsh, and C. Y. Peng, 1989: A case study of wave–current interaction near an oceanic front. *J. Geophys. Res.,* **94** (C11), 16 189–16 200.

——, B. Holt, and P. W. Vachon, 1991a: Wave propagation in the marginal ice zone: Model predictions and comparisons with buoy and synthetic aperture radar data. *J. Geophys. Res.,* **96** (C3), 4605–4621.

——, P. W. Vachon, and C. Y. Peng, 1991b: Observation of wave refraction at an ice edge by synthetic aperture radar. *J. Geophys. Res.,* **96** (C3), 4803–4808.

——, ——, ——, and A. S. Bhogal, 1992: Wave attenuation in the marginal ice zone during LIMEX. *Atmos.–Ocean,* **30**, 192–206.

——, S. Häkkinen, and C. Y. Peng, 1993: Wave effects on ocean–ice interaction in the marginal ice zone. *J. Geophys. Res.,* **98** (C6), 10 025–10 036.

——, C. Y. Peng, and J. D. Shumacher, 1994: Wave–current interaction study in the Gulf of Alaska for the detection of eddies by synthetic aperture radar. *J. Geophys. Res.,* **99** (C5), 10 075–10 085.

——, ——, and T. J. Weingartner, 1994: Ocean–ice interaction in the marginal ice zone using synthetic aperture radar imagery. *J. Geophys. Res.,* **99** (C11), 22 391–22 400.

Lyzenga, D. R., 1986: Numerical simulation of synthetic aperture radar image spectra for ocean surface waves. *IEEE Trans. Geosci. Remote Sens.,* **24**, 863–872.

——, 2002: Unconstrained inversion of wave height spectra. *IEEE Trans. Geosci. Remote Sens.,* **40***,* 261–270.

——, R. A. Shuchman, J. D. Lyden, and C. L. Rufenach, 1985: SAR imaging of waves in water and ice: Evidence for velocity bunching. *J. Geophys. Res.,* **90** (C1), 1031–1036.

Mastenbroek, C., and C. F. de Valk, 2000: A semiparametric algorithm to retrieve ocean surface wave spectra from synthetic aperture radar. *J. Geophys. Res.,* **105** (C2), 3497–3516.

McLeish, W., and D. B. Ross, 1983: Imaging radar observations of directional properties of ocean surface waves. *J. Geophys. Res.,* **88** (C7), 4407–4419.

Monaldo, F. M., and R. C. Beal, 1986: Limitations of the Seasat SAR in high sea states. *Wave Dynamics and Radio Probing of the Ocean Surface*, O. M. Phillips and K. Hasselmann, Eds., Plenum, 423–442.

——, and D. R. Lyzenga, 1986: On the estimation of wave slope and wave height-variance spectra from SAR imagery. *IEEE Trans. Geosci. Remote Sens.,* **24**, 543–551.

——, and ——, 1988: Comparison of Shuttle Imaging Radar-B ocean surface wave image spectra with linear model predictions. *J. Geophys. Res.,* **93***,* 15 374–15 388.

——, and R. C. Beal, 1995: Real-time observations of southern ocean surface wave fields from the shuttle imaging radar. *IEEE Trans. Geosci. Remote Sens.,* **33**, 942–949.

——, and ——, 1998: Comparison of SIR-C SAR wavenumber spectra with WAM model predictions. *J. Geophys. Res.,* **103***,* 18 815–18 825.

——, T. G. Gerling, and D. G. Tilley, 1993: Comparison of SIR-B SAR wave image spectra with wave model predictions: Implications on the SAR modulation transfer function. *IEEE Trans. Geosci. Remote Sens.,* **31**, 1199–1209.

Munk, W. H., G. R. Miller, F. E. Snodgrass, and N. F. Barber, 1963: Directional recordings of swell from distant storms. *Philosl. Trans. Roy. Soc. London,* **255A**, 505–583.

Newyear, K., and S. Martin, 1999: Comparison of laboratory data with a viscous two-layer model of wave propagation in grease ice. *J. Geophys. Res.,* **104** (C4), 7837–7840.

Niedermeier, A., J. C. Nieto Borge, and S. Lehner, 2002: A wavelet based algorithm to extract ocean wave groupiness from ERS-1/2 and ENVISAT SAR-imagette amplitude data. *IEEE Trans. Geosci. Remote Sens.*, submitted.

Plant, W. J., and L. M. Zurk, 1997: Dominant wave directions and significant wave heights from synthetic aperture radar imagery of the ocean. *J. Geophys. Res.,* **102***,* 3473–3482.

Pond, S., and G. L. Pickard, 1983: *Introductory Dynamical Oceanography.* 2d. ed. Pergamon Press, 329 pp.

Raney, R. K., 1971: Synthetic aperture radar imaging of moving targets. *IEEE Trans. Aerosp. Electron. Syst.,* **7***,* 499–505.

——, 1980: SAR response to partially coherent phenomena. *IEEE Trans. Antennas Propag.,* **28**, 777–787.

——, and P. W. Vachon, 1988: SAR imaging of ocean surface waves from an airborne platform: Focus and tracking issues. *J. Geophys. Res.,* **93** (C10), 12 475–12 486.

Shuchman, R. A., C. L. Rufenach, and O. M. Johannessen, 1994: Extraction of marginal ice zone thickness using gravity wave imagery. *J. Geophys. Res.,* **99** (C1), 901–918.

Squire, V. A., 1995: Geophysical and oceanographic information in the marginal ice zone from ocean surface wave measurements. *J. Geophys. Res.,* **100** (C1), 997–998.

——, J. P. Dugan, P. Wadhams, P. J. Rottier, and A. K. Liu, 1995: Of ocean surface waves and sea ice. *Annu. Rev. Fluid Mech.*, **27**, 115–168.

Swift, C. T., and L. R. Wilson, 1979: Synthetic aperture imaging of ocean surface waves. *IEEE Trans. Antennas Propag.,* **27**, 725–729.

Tilley, D. G., 1986: Use of speckle for determining the response characteristics of Doppler imaging radars. *Opt. Eng.,* **25***,* 772–779.

——, and R. C. Beal, 1994: ERS-1 and Almaz estimates of directional wave spectra conditioned by simultaneous aircraft SAR and buoy measurements. *Atmos.–Ocean,* **32**, 113–142.

Tucker, M. J., 1985: The imaging of waves by synthetic-aperture radar: The effects of surface motion. *Int. J. Remote Sens.,* **6**, 1075–1089.

Vachon, P. W., and R. K. Raney, 1991: Resolution of the ocean surface wave propagation direction in SAR imagery. *IEEE Trans. Geosci. Remote Sens.,* **29**, 105–112.

——, and J. C. West, 1992: Spectral estimation techniques for multilook SAR images of ocean surface waves. *IEEE Trans. Geosci. Remote Sens.,* **30**, 568–577.

——, R. B. Olsen, C. E. Livingstone, and N. G. Freeman, 1988: Airborne SAR observations of ocean surface waves during LEWEX: Some initial results. *IEEE Trans. Geosci. Remote Sens.,* **26**, 549–562.

——, ——, H. E. Krogstad, and A. K. Liu, 1993: Airborne synthetic aperture radar observations simulations for waves in ice. *J. Geophys. Res.,* **98** (C9), 16 411–16 425.

——, H. E. Krogstad, and S. Paterson, 1994: Airborne and spaceborne SAR observations of ocean surface waves. *Atmos.–Ocean,* **32**, 83–112.

Vesecky, J. F., and R. H. Stewart, 1982: The observation of ocean surface phenomena using imagery from the Seasat synthetic aperture radar: An assessment. *J. Geophys. Res.,* **87***,* 3397–3430.

Wadhams, P., 2000: *Ice in the Ocean*. Gordon and Breach, 351 pp.

Wadhams, P., and B. Holt, 1991: Waves in frazil and pancake ice and their detection in Seasat synthetic aperture radar imagery. *J. Geophys. Res.,* **96** (C5), 8835–8852.

Wright, J. W., 1960: Backscattering from capillary waves with application to sea clutter. *IEEE Trans. Antennas Propag.,* **14**, 749–754.

Young, I. R., 1999: Seasonal variability of the global ocean wind and wave climate. *Int. J. Climatol.,* **19**, 931–950.